

1 **Performance of AIRS ozone retrieval over the central Himalayas: ~~Case studies~~Use of**
2 **~~biomass burning, downward ozone transport~~ozonesonde and ~~radiative forcing using long-~~**
3 **~~term observations~~other satellite dataset**

4
5
6 Prajwal Rawat^{1,5}, Manish Naja¹, Evan Fishbein², Pradeep K. Thapliyal³, Rajesh Kumar⁴, Piyush
7 Bhardwaj⁴, Aditya Jaiswal¹, Sugriva N. Tiwari⁵, Sethuraman Venkataramani⁶, Shyam Lal⁶

8
9
10
11 ¹ Aryabhata Research Institute of Observational Sciences (ARIES), Nainital, 263001, India

12 ² NASA Jet Propulsion Laboratory, Pasadena, CA 91109, USA

13 ³ Space Applications Centre, ISRO, Ahmedabad 380015, India

14 ⁴ National Center for Atmospheric Research (NCAR) Boulder, CO 80307, USA

15 ⁵ DDU Gorakhpur University, Gorakhpur 273009, India

16 ⁶ Physical Research Laboratory (PRL), Ahmedabad, 380009, India

17
18
19
20
21 **Corresponding author: Manish Naja (manish@aries.res.in)**

26

27

28 **Short Summary:**

29 Satellite based ozone observations have gained wide importance due to their global coverage.
30 However, satellite retrieved products are indirect and need to be validated, particularly over
31 mountains. Here, ozonesondes launched from a Himalayan site are utilized to assess the AIRS
32 ozone retrieval. AIRS is shown to overestimate ozone in the upper troposphere and lower
33 stratosphere, while the differences with ozonesonde are lower in the middle troposphere and
34 middle stratosphere.

35

36

37

38

39

40

41

42

43

44

45

46

47

48

49

50

51

52

53 **Abstract**

54 Data from 242 ozonesondes launched from ARIES Nainital (29.40° N, 79.50° E, and 1793 m
55 elevation) are used to evaluate the Atmospheric Infrared Sounder (AIRS) version 6 ozone profiles
56 and total column ozone during the period 2011-2017 over the central Himalaya. The AIRS ozone
57 products are analyzed in terms of retrieval sensitivity, retrieval biases/errors, and ability to retrieve
58 the natural variability of columnar ozone, which has not been done so far from the Himalayan
59 region having complex topography. For a direct comparison, averaging kernels information is used
60 to account for the sensitivity difference between the AIRS and ozonesonde data. We show that
61 AIRS has lower differences with ozonesonde in the lower and middle troposphere and stratosphere
62 with nominal underestimations of less than 20%. However, in the upper troposphere and lower
63 stratosphere (UTLS), we observe a considerable overestimation of the magnitude, as high as 102%.
64 The weighted statistical error analysis of AIRS ozone shows higher positive bias and standard
65 deviation in the upper troposphere of about 65% and 25%, respectively. Similar to AIRS, Infrared
66 Atmospheric Sounding Interferometer (IASI) and Cross-track Infrared Sounder (CrIS) are also
67 able to produce ozone peak altitudes and gradients successfully. However, the statistical errors are
68 again higher in the UTLS region that are likely related to larger variability of ozone, lower ozone
69 partial pressure and inadequate retrieval information on the surface parameters. Furthermore,
70 AIRS fails to capture the monthly variation of the total ozone column, with a strong bimodal
71 variation, unlike unimodal variation seen in ozonesonde and Ozone Monitoring Instrument (OMI).
72 In contrast, the UTLS and the tropospheric ozone columns are in reasonable agreement. Increases
73 in the ozone values by 5 - 20% after biomass burning and during events of downward transport
74 are captured well by AIRS. Ozone radiative forcing (RF) derived from total column ozone using
75 ozonesondes data (4.86 mWm^{-2}) matches well with OMI (4.04 mWm^{-2}), while significant RF
76 underestimation is seen in AIRS (2.96 mWm^{-2}). The fragile and complex landscapes of the
77 Himalayas are more sensitive to global climate change and establishing such biases and error
78 analysis of space-borne sensors will help study the long-term trends and estimate accurate radiative
79 budgets.

80

81

82

83

84 1. Introduction

85 Atmospheric ozone is an essential trace gas that plays a crucial role in the atmospheric oxidizing
86 chemistry, air quality, and earth's radiative budget. The stratospheric ozone absorbs harmful solar
87 ultraviolet radiation and protects biological life on earth, whereas tropospheric ozone, being a
88 secondary air pollutant (~~Logan et al., 1985; Pitts and Pitts, 1997; e.g.~~ Pierce et al., 2009; Monks et
89 al., 2015; Lelieveld et al., 2018) and greenhouse gas, contributes to global warming and can harm
90 human health and crops when present in higher concentrations near the surface (Fishman et al.,
91 1979; Ebi and McGregor 2008; Lal et al., 2017). Different radiative forcing of ozone from the
92 stratosphere (cooling) to the troposphere (heating) (Lacis et al., 1990; Wang et al., 1993; Forster
93 et al., 2007; Hegglin et al., 2015) demonstrate its potential importance as an atmospheric climate
94 gas (Shindell et al., 2012; Thornhill et al., 2021). Hence, information regarding precise long-term
95 variability in global ozone distribution is vital for better characterizing atmospheric chemistry and
96 global climate changes (~~McPeters et al., 1994;~~ Kim et al., 1996; Myhre et al., 2017).

97
98 In recent decades, observations of ozone from space-borne sensors (microwave limb sounding,
99 UV-VIS, and IR) have become an increasingly robust tool for global and higher temporal
100 monitoring (~~Fishman et al., 1986; Munro et al., 1998; e.g.~~ Bhartia et al., 1996; Foret et al., 2014).

101 This increases our ability to analyze various influences of human activities on the atmospheric
102 chemical composition, including ozone, study their long-term impact on climate (Fishman et al.,
103 1987; ~~Fry et al., 2012;~~ Tarasick et al., 2019; Thornhill et al., 2021), and estimate reliable radiative
104 budgets (Hauglustaine and Brasseur 2001; Gauss et al., 2003; Aghedo et al., 2011). However, the
105 space-based sensors are indirect and measure the atmospheric composition based upon specific
106 algorithms utilizing radiative transfer models and a-priori information. Hence, the retrieval outputs

107 need to be evaluated with certain reference instruments for establishing the credibility and better
108 utilization of space-borne data.

109

110 The Himalayas, a complex terrain region, has the largest abundance of ice sheets outside polar
111 regions that impacts global/regional radiative budgets and climate pervasively (e.g., Lawrence and
112 Lelieveld, 2010; Cristofanelli et al., 2014; ~~Zhang et al., 2015~~). Very sparse in-situ and ground-
113 based observations in this region, along with inadequate information on the surface parameters,
114 makes it difficult to retrieve atmospheric composition from space-borne instruments. This is
115 because the ozone weighting function, a measure of the retrieval sensitivity and a fundamental
116 retrieval component, depends upon various atmospheric parameters like surface temperature,
117 surface emissivity, and terrain height (Rodgers et al., 1976, 1990; Bai et al., 2014), which is not
118 uniform over the foot-print size of the AIRS (~ 13 km x 13 km) ~~over~~in the Himalayas. Usually,
119 the ozone weighting function has a shorter integrating path over the elevated terrain regions, which
120 follows a smaller weighting function and provides lesser sensitivity and higher errors in the final
121 retrievals (Coheur et al., 2005; Bai et al., 2014).

122

123 The Atmospheric Infrared Sounder (AIRS) onboard the Aqua satellite has been providing reliable
124 vertical profiles of ozone, temperature, water vapor, and other trace gases globally twice a day
125 since 2002. Numerous validation studies of AIRS retrieved ozone have been carried out for
126 different versions since it started operating (2002). For example, Bian et al. (2007) studied AIRS
127 version 4 over Beijing and discussed the potential agreements (within 10%) between AIRS and
128 ozonesonde (GPSO3) ozone, particularly in the upper troposphere and lower stratosphere (UTLS)
129 region with the capability of AIRS to identify various Stratosphere-Troposphere Exchange (STE)

130 and transient convective events. Similarly, a study over Boulder and Lauder by Monahan et al.
131 (2007) using a similar AIRS version showed despite the larger biases in the lower and middle
132 tropospheric region, the retrieval algorithm captures the ozone variability very effectively with a
133 positive correlation of more than 70%. However, that study suggested a need for tropopause-
134 adjusted coordinates in the a-priori profiles. Both these studies (Bian et al., 2007; Monahan et al.,
135 2007) show larger biases in AIRS ozone in the lower and middle tropospheric regions; however,
136 shifts in retrieval biases and errors were seen towards the UTLS region in version 5 (Divakarla et
137 al., 2008), apart from significant improvements in the lower troposphere. The retrieval
138 methodology has also changed significantly between V4 and V5. Version 4 or earlier used
139 regression retrieval as the first guess in physical retrieval, while later versions used a climatology-
140 based first guess for the physical retrieval based on other works (McPeters et al., 2007). Also,
141 radiative transfer models, selected channel sets, and clarified quality indicators have been modified
142 and improved in all successive versions.

143

144 The AIRS ozone retrieval in V5 has improved significantly with retrieval biases and root mean
145 square error (RMSE) less than 5% and 20%, respectively (Divakarla et al., 2008), over the tropical
146 regions. However, there is not much discussion and studies of the assessment for AIRS ozone over
147 the Himalayas' complex terrain, where retrieval is expected to be erroneous due to large surface
148 variability within its footprint. Also, most of the previous studies (Bian et al., 2007; Divakarla et
149 al., 2008; Pittman et al., 2009) did not utilize the averaging kernels information of the AIRS that
150 is vital for satellite evaluation. Recently, ozonesonde observations are also utilized to evaluate the
151 total and tropospheric ozone column from various satellite retrievals over the Andes Mountains.
152 This study shows nominal differences between satellite and ozonesonde for the total ozone

153 column, while the tropospheric ozone column shows a difference of up to 32.5% (Cazorla and
154 Herrera, 2022). Such evaluation studies, along with the present analysis, comprehend the possible
155 differences between satellite and truth observations and advise towards the trustworthiness of
156 satellite data over the complex mountain regions.

157
158 HereSpecifically, here, the evaluation of AIRS version 6, which entirely depends upon the infra-
159 red (IR) observations after the failure of the AMSU sensor, is presented in terms of statistical
160 analysis and ability to retrieve the natural variability of ozone at various altitudes over the central
161 Himalayan region using in-situ ozonesonde observations convolved with AIRS averaging kernels.
162 Additionally, the present study assessed the AIRS retrieval algorithm using IASI and CrIS radiance
163 information for one year. AIRS columnar ozone (i.e., total, UTLS, and tropospheric columns) is
164 also assessed with ozonesonde, OMI, and Microwave Limb Sounder (MLS) observations. AIRS
165 has a long-term data set for ozone and meteorological parameters, establishing such biases and
166 error analysis is essential to make meaningful use of its data to characterize the Himalayan
167 atmosphere, study the trends, radiative budgets, perform the model evaluation and data
168 assimilation over this region.

170 **2 Data and Methodology**

171 **2.1 Data Description**

172 **2.1.1 AIRS**

173 Atmospheric Infrared Sounder (AIRS) onboard Aqua satellite, in the sun synchronous polar orbit
174 at 705 km altitude, is a hyperspectral thermal infrared grating spectrometer with equatorial
175 crossings at ~13:30 local time (LT). It is a nadir scanning sensor that was deployed in orbit on

176 May 4, 2002. AIRS, along with its partner microwave instrument, the Advanced Microwave
177 Sounding Unit (AMSU-A), represents the most advanced atmospheric sounding system placed in
178 space using cutting-edge infrared and microwave technologies. These instruments together
179 observe the global energy cycles, water cycles, climate variations, and greenhouse gases, however,
180 after AMSU failure, the retrieval now mostly depends upon the AIRS IR observations. The AIRS
181 infrared spectrometer acquires 2378 spectral samples at resolutions ($\lambda/\Delta\lambda$) ranging from 1086 to
182 1570 cm^{-1} , in three bands: $3.74\text{ }\mu\text{m}$ to $4.61\text{ }\mu\text{m}$, $6.20\text{ }\mu\text{m}$ to $8.22\text{ }\mu\text{m}$, and $8.8\text{ }\mu\text{m}$ to $15.4\text{ }\mu\text{m}$
183 (Fishbein et al., 2003; Pagano et al., 2003). The independent channels of AIRS permit retrieval of
184 various atmospheric states and constituents depending upon their corresponding spectral response,
185 even in the presence of a 90% cloud fraction (Susskind et al., 2003; Maddy and Barnet, 2008). In
186 this study, we have used Level 2 Support physical products of AIRS (AIRS2SUP). The AIRS2SUP
187 files (~240 granules/day) possess extra information over the standard AIRS files, e.g., information
188 on averaging kernel and degree of freedom, including vertical profiles at 100 pressure levels,
189 against just 28 in the standard product.

190

191 The support product profiles contain 100 levels between 1100 and 0.016 mbar. While it has a
192 higher vertical resolution, the vertical information content is no greater than the standard product.
193 The information on averaging kernels and degree of freedoms (DOFs) is utilized to understand the
194 retrieved products more comprehensively. The DOFs of ozone, a measure of significant eigen
195 functions used in the AIRS retrieval, have an average value of 1.36 over the tropical latitude band
196 (Maddy and Barnet 2008) (Table S1), while over the balloon collocated region, an average DOFs
197 of 1.62 is observed (Figure S1). In the present study, the AIRS data is flagged as best quality when
198 the cloud fraction is less than 80%, and the degrees of freedom (DOF) are greater than 0.04.

199 However, analysis of cloud fraction over our collocated region shows (Figure S2) only 7% of
200 observations during 2011 - 2017 had a cloud fraction of more than 80%.

201

202

203

204 **2.1.2 IASI (NOAA/CLASS)**

205 The Infrared Atmospheric Sounding Interferometer (IASI) onboard MetOp satellites, with a
206 primary focus on meteorology than climate and atmospheric chemistry monitoring, is a nadir
207 viewing Michelson interferometer (Clerbaux et al., 2007). The first MetOp satellite was launched
208 in October 2006 (MetOp-A), and IASI was declared operational in July 2007. MetOp is a polar
209 sun-synchronous satellite having descend and ascend nodes at 09:30 and 21:30 LT, respectively.
210 IASI measures in the IR part of the EM spectrum at a horizontal resolution of 12 km at nadir up to
211 40 km over a swath width of about 2,200 km. IASI covers an infra-red spectral range between 3.7
212 to 15.4 μm with a total of 8461 spectral channels, out of which 53 channels around 9.6 μm are
213 utilized for ozone retrieval. IASI level 2 ozone products provided by NOAA National
214 Environmental Satellite Data and Information Service (NESDIS) Center for Satellite Application
215 and Research (STAR) are used in this study. The IASI (NOAA/CLASS) ozone product is retrieved
216 based on the AIRS algorithm and has various quality control flags (Table S2). Only QC=0 data
217 which represents a successful IR ozone retrieval, is used.

218

219 **2.1.3 CrIS/ATMS (NUCAPS)**

220 The Cross-track Infrared Sounder (CrIS) and Advanced Technology Microwave Sounder (ATMS)
221 onboard the Suomi NPP satellite were launched in 2011 to feature the high spectral-resolution

222 (“hyperspectral”) observations of earth’s atmosphere. The CrIS instrument is an advanced Fourier
223 transform spectrometer with an ascending node 13:30 LT and flies at a mean altitude of 824 km
224 and performs fourteen orbits per day. It measures high-resolution IR spectra in the spectral range
225 650 - 2550 cm^{-1} with a total of 1305 channels. The ATMS is a microwave sounder with a total of
226 22 channels ranging from 23 to 183 GHz. These two instruments, CrIS and ATMS, operate in an
227 overlapping field-of-view (FOV) formation, with ATMS FOVs re-sampled to match the location
228 and size of the 3×3 CrIS FOVs for retrieval under clear to partly cloudy conditions. Here the
229 NUCAPS algorithm-based ozone product of CrIS is utilized. The NOAA Unique CrIS/ATMS
230 Processing System (NUCAPS) is a heritage algorithm developed by the STAR team based on the
231 AIRS retrieval algorithm (Susskind et al., 2003, 2006). The NOAA implemented NUCAPS
232 algorithm is a modular architecture that was specifically designed to be compatible with multiple
233 instruments. The same retrieval algorithms are currently used to process the AIRS/AMSU suite
234 (operations since 2002), the IASI/AMSU/MHS suite (operational since 2008), and now the
235 CrIS/ATMS suite (approved for operations in January 2013). Here again, various quality controls
236 for retrieved data are provided by the NUCAPS science algorithm team, and we used QC=0 for
237 lesser discrepancies in our evaluation (Table S2). These research products follow a similar retrieval
238 algorithm as developed by the AIRS science team, which gives us further opportunity to assess the
239 AIRS retrieval algorithm for IASI and CrIS radiances.

240

241 **2.1.4 Ozonesonde**

242 EN-SCI electrochemical concentration cell (ECC) ozonesondes and GPS-radiosondes (iMet) have
243 been launched from the Aryabhata Research Institute of Observational Sciences (ARIES) (29.4°
244 N, 79.5° E, and 1793 m elevation) Nainital (Figure 1), a high-altitude site in central Himalaya,

245 since 2011 (Ojha et al., 2014; Rawat et al., 2020), the only facility in the Himalayan region having
246 regular launchings. ECC ozonesonde relies on the oxidation reaction of ozone with potassium
247 iodide (KI) solution (Komhyr et al., 1967, 1995) to measure ozone partial pressure in the ambient
248 atmosphere. The typical vertical resolution of ozonesonde is about 100 - 150 m and has a precision
249 of better than $\pm 3 - 5 \%$ with an accuracy of about $\pm 5 - 10 \%$ up to 30 km altitude under standard
250 operating procedures (Smit et al., 2007; Smit & ASOPOS Panel, 2020). The ozonesonde is
251 connected to iMet-radiosonde via a V7 electronic interface, where radiosonde consists of GPS,
252 PTU, and a transmitter to transmit signals to the ground.

253
254 The ozonesonde sensor's successful performance is assured before launch (about 3 - 7 days before
255 launch) as part of advance preparation and during the day of launch by maintaining and reviewing
256 the records for background current, pump flow rate, response time, etc. The ozonesonde data
257 quality is further assured by estimating these ECC ozonesondes' total ozone normalization factor
258 with collocated OMI total ozone. [\(Figure S3\)](#). These factors are well within the ASOPOS
259 recommendation with an average of 1.0 ± 0.04 , which implies the reasonable quality of these
260 ozonesondes (Smit & ASOPOS Panel, 2020). Additionally, ozonesonde observations from present
261 site have also been utilized in SUSKAT (Bhardwaj et al., 2018) and StratoClim (Brunamonti et
262 al., 2018) field campaigns and in other studies (Ojha et al., 2014). Further, owing to higher
263 accuracy and in-situ measurement, ozonesonde has been widely used worldwide for satellite and
264 model validation ([Monahan et al., 2007](#); Divakarla et al., 2008; ~~Nassar et al., 2008~~; ~~Monahan et~~
265 ~~al., 2007~~; Kumar et al., 2012a, 2012b; Dufour et al., 2012; Verstraeten et al., 2013; Boynard et al.,
266 2016; Rawat et al., 2020). Both the ascending and descending data were recorded by ozonesonde,
267 however, due to time lag in descending records, only ascending data is utilized (Lal et al., 2013,

268 2014; Ojha et al., 2014). The data is collected at the interval of about 10 meters which is averaged
269 over 100 meters interval using a 3σ filter that removes the outlier values (Srivastava et al., 2015;
270 Naja et al., 2016).

271

272 **2.1.5 Other Auxiliary Data**

273 Additionally, collocated and concurrent OMI and MLS observations are also used to study the
274 tropospheric ozone, UTLS, and total ozone column due to their reasonable sensitivity and well-
275 validated retrievals (Veefkind et al., 2006; Ziemke et al., 2006; Fadnavis et al., 2014; Wang et al.,
276 2021). The tropospheric ozone column obtained from OMI and MLS is based on the residual
277 method, which depends upon the collocated difference between the MLS stratospheric ozone
278 column and OMI total ozone column, which is described in detail by Ziemke et al. (2006).
279 Furthermore, the MLS version 4 data is utilized for the UTLS column above 261 hPa due to its
280 credibility in this range for scientific applications (Livesey et al., 2013; Schwartz et al., 2015).
281 Moreover, for fair statistical analysis between ozonesonde and MLS ozone profile, Gaussian
282 smoothing is applied to ozonesonde with full width at half maximum equal to typical upper
283 tropospheric vertical resolution ($\sim 2 - 4$ km) of MLS (Livesey et al., 2013). The best quality data
284 of MLS with data flags, i.e., status=even, quality > 0.6 , and convergence < 1.18 , is utilized (Ziemke
285 et al., 1998; Barre et al., 2012). However, a slightly different collocation criterion of $3^\circ \times 3^\circ$ grid
286 box and daytime collocation is utilized for MLS in this work due to coarser resolution and to get
287 sufficient matchups.

288

289 **2.2 Methods of Analysis**

290 The balloon launch time is mostly around 12:00 IST (Indian Standard Time, which is 5.5 hours
291 ahead of GMT). The Aqua satellite comes over the India around 1:30 pm and 1:30 am IST. Hence
292 for collocation, only noontime (ascending) data (or ± 3 hours of balloon launch) with $1^\circ \times 1^\circ$ spatial
293 collocation were chosen in this evaluation. However, for some days, there was no noontime
294 granule in AIRS retrieval (nearly 35 out of total 242 soundings), then we used a loose collocation
295 of ± 1 day. However, no significant changes were seen after such flexible collocation. Most of the
296 ozonesondes have burst altitudes near 10 hPa, hence AIRS ozone profiles are evaluated from
297 surface to 10 hPa.

298
299 Although suitable collocation criteria have been defined for a fair comparison, still different
300 vertical resolutions of the two data sets (ozonesonde ~ 100 m and AIRS $\sim 1-5$ km) make the
301 meaningful comparison difficult (Maddy and Barnet, 2008; Verstraeten et al., 2013; Boynard et
302 al., 2016). The difference in vertical resolution and retrieval sensitivity must be accounted for a
303 meaningful comparison. Though there is no perfect way to remove the error arising from the
304 different vertical resolutions of the two measurements, still utilizing the averaging kernel
305 smoothing or Gaussian smoothing, the error is minimized. Various groups have used the satellite
306 averaging kernels smoothing to compare satellite measurements with ozonesonde (Zhang et al.,
307 2010; Verstraeten et al., 2013; Boynard et al., 2016, 2018), while Gaussian smoothing (Wang et
308 al., 2020) and broad layer columns (Nalli et al., 2017) are also utilized. In the present analysis,
309 averaging kernel smoothing is utilized. ~~First, ozonesonde data were interpolated at all AIRS~~
310 ~~Radiative Transfer Algorithm (RTA) layers from surface to burst altitude, then ozonesonde~~
311 ~~profiles were smoothed according to the AIRS averaging kernel and a priori profile (ML~~
312 ~~climatology), leading to a vertical profile [ozonesonde (AK)] representing what AIRS would have~~

313 measured for the same ozonesonde sampled atmospheric air mass in the absence of any other error
 314 affecting satellite observations. According to (Rodgers and Connor (, 2003), the smoothing of the
 315 true state can be characterized as follows:

$$316 \quad X_{est} = X_0 + A' (X_{sonde} - X_0) \quad (1)$$

317 The AIRS provides averaging kernels information at 9 pressure levels (Figure 2b) whereas the
 318 AIRS RTA has 100 pressure levels. So following ozone vertices (Table S3) and formulating
 319 trapezoid matrix (Figure 2a, the) and explained with details regarding the calculation of trapezoid
 320 matrices are given in AIRS/AMSU/HSB Version 6 Level 2 Product Levels, Layers and
 321 Trapezoids), we convert 9 levels AIRS averaging kernels to 100 levels averaging kernels using
 322 following defined operation.

$$323 \quad A' = F \times A_{trapezoid} \times F' \quad (2)$$

324 Where $A_{trapezoid}$ and F are averaging kernel matrices and trapezoid matrices (F' is pseudo-inverse
 325 of F). $A_{trapezoid}$ is a given product, while F is calculated for given ozone vertices (Table S3).

326 Further, in the thermal IR spectrum in supplementary section 1.1. Generally, the contribution of
 327 ozone or any other trace gas towards emission/absorption of IR radiation in the radiative transfer
 328 equation depends on the exponent of layer integrated column amounts (Maddy and Barnet, 2008).
 329 Hence logarithmic changes in layer column density are more linear than absolute changes. So
 330 logarithmic equations are used instead of Eq. 1 for smoothing ozonesonde datais utilized in the
 331 present study: as follows:

$$332 \quad \ln (X_{est}) = \ln (X_0) + A' \{ \ln (X_{sonde}) - \ln (X_0) \} \quad (31)$$

333 Where X_{est} , X_{sonde} , and X_0 are smooth ozonesonde or ozonesonde (AK), true ozonesonde, and first
 334 guess (ML climatology) profiles, respectively. Knowing the nature of convolution from Eq. 1 and

335 3, it can be observed that the ozonesonde (AK) or smooth ozonesonde will have more weights
336 toward a-priori profiles when satellite retrieval is poor or AKs approaches zero values.

337 More details on the calculation of averaging kernels, [ozone vertices \(Table S3\)](#), and [trapezoid](#)
338 [matrix](#) can be found in AIRS documents (AIRS/AMSU/HSB Version 6 Level 2 Product Levels,
339 Layers and Trapezoids) ~~or~~ [and](#) in available literature (Maddy and Barnett, 2008; Irion et al., 2018).
340 A typical averaging kernels matrix and other parameters are shown in Figure 2. Figure 2a shows a
341 typical trapezoid matrix, Figure 2b shows the averaging kernels at 9 pressure levels, Figure 2c
342 shows constructed averaging kernels at 100 RTA layers, and Figure 2d shows an example of the
343 different ozone profiles convolved with AKs on 15 June 2011 over the observation site.

344

345 **2.3 Statistical Analysis**

346 ~~The~~ [Furthermore, the](#) error analysis for AIRS retrieval with interpolated and smoothed ozonesonde
347 is based on Nalli et al. (2013, 2017). Bias, root mean squared error (RMSE), and standard deviation
348 (STD) are studied at various RTA vertical levels from the surface to 10hPa over the Himalayan
349 region. ~~The finer spatio-temporal collocation utilized here has further minimized the uncertainty~~
350 ~~and error in the evaluation. Since the observation site (29.4° N, 79.5° E) is at a latitude lower than~~
351 ~~45°; hence there is a lesser overlap of satellite passes, and mostly a few nadir scans are close to the~~
352 ~~observation site (mostly daytime granules in the range of 75 to 85). Hence all the daytime~~
353 ~~observations of AIRS are close to ± 3 hours of temporal collocation to the ozonesonde launch and~~
354 ~~possess a lesser chance of time mismatch~~ [We have used the \$W_2\$ weight factor in statistical analysis](#)
355 [as suggested by other sounder science team \(Nalli et al., 2013, 2017\) and explained in](#)
356 [supplementary section 1.2.](#)

357

Given the collocated ozone mixing ratio profiles for satellite, ozonesonde (AK), and in-situ truth (ozonesonde) observations, the statistical errors are calculated as follows—

$$\text{RMSE} (\Delta O_i) = \sqrt{\frac{\sum_{j=1}^{j=n} W_{tj} \times (\Delta O_{tj})^2}{\sum_{j=1}^{j=n} W_{tj}}} \quad (4)$$

$$\text{Bias} (\Delta O_i) = \frac{\sum_{j=1}^{j=n} W_{tj} \times (\Delta O_{tj})}{\sum_{j=1}^{j=n} W_{tj}} \quad (5)$$

Here l runs over different RTA layers and j runs for all collocated profiles, $\Delta O_{i;j}$ the fractional deviation is taken to be the absolute deviation divided by the observed value. Where $\Delta O_{i;j} = \left(\frac{\theta_{tj}^R - \theta_{tj}^T}{\theta_{tj}^T} \right)$, θ^T and θ^R are ozonesonde/ozonesonde (AK) and satellite retrieved ozone mixing ratio, respectively. $W_{i;j}$ is the weighting factor and assumes one of three forms $W_0=1$, $W_1=\theta^R$ and $W_2 = (\theta^R)^2$ and for ozone to minimize skewing impact due to large variation in mixing ratio at different altitudes, we have used the W_2 -weight factor as suggested by other sounder science team (Nalli et al., 2013, 2017). The Standard deviation (STD) is then calculated by the square root of difference between RMSE and biases square at different RTA levels. Further to check the strength of the linear relationship between the satellites retrieved data and ozonesonde data the square of Pearson's correlation coefficient is also calculated.

2.4 Estimation of Columnar Ozone

The Additionally, the total column ozone (TCO) from ozonesonde is calculated by integrating the ozone mixing ratio from the surface to burst altitude and then adding residual ozone above burst altitude. Here the residual ozone is obtained from satellite-derived balloon-burst climatology

379 (BBC) (McPeters and Labow, 2012; Stauffer et al., 2022). ~~The~~ and the discrete integration ~~for~~
380 ~~calculation of total ozone column (DU) between defined boundaries is performed as follows:~~

$$381 \quad \text{Total column ozone} = 10^7 \times \left(\frac{RT_0}{g_0 P_0} \right) \times \sum_{j=1}^{j=n} 0.5 \times (VMR[i] + VMR[i + 1]) \times (P[i] - P[i + 1]) \quad (6)$$

382
383 ~~Where P is ambient pressure explained in hPa, VMR volume mixing ratio of ozone in ppbv, R (=~~
384 ~~287~~supplementary section 1.3 $\text{JK g}^{-1} \text{K}^{-1}$) ~~gas constant, g_0 (= 9.88 ms^{-2}), P_0 (= 1.01325×10^5 Pa) and~~
385 ~~T_0 (= 273.1 K) standard temperature.~~

386 ~~The UTLS ozone column (DU) is also calculated using Eq. (6), where the UTLS region is defined~~
387 ~~between 400 hPa to 70 hPa (Bian et al., 2007). Additionally, Similarly,~~ the tropospheric ozone
388 column (~~DU~~) is calculated ~~for ozonesonde utilizing Eq. (6) with boundaries by integrating ozone~~
389 ~~from the surface to the lapse rate tropopause (LRT),) and UTLS column is calculated between 400~~
390 ~~hPa to 70 hPa (Bian et al., 2007).~~ The tropopause height from balloon-borne observations is
391 estimated using the lapse rate method as well as the AIRS-derived tropopause is used and shown
392 in Figure 3. ~~However, for OMI and MLS tropospheric ozone residual method is used, which~~
393 ~~calculates~~In addition, the tropospheric ozone column ~~by subtracting the OMI total column~~ from
394 ~~MLS stratospheric ozone column~~OMI/MLS observation is also utilized due to its reliable data
395 (Hudson et al., 1998; Ziemke et al., 2006).

397 **3. Results and Discussion**

398 **3.1 Ozone Distribution along Balloon Trajectory: Ozonesonde and AIRS**

399 The distributions of ozone along the balloon tracks obtained using all ozone soundings data during
400 four seasons are shown in Figure 4. The nearest swath of AIRS ozone observations is interpolated
401 to the balloon locations and altitudes. Altitude variations of the balloon along longitude are

402 shown in Figure [S3S4](#). The balloons drift to a very long-distance during winter, followed by
403 autumn and spring. During these seasons, balloons often reach Nepal also. The wind reversal took
404 place during the summer-monsoon when the balloon drifts towards IGP regions (Figure 4). The
405 distributions of ozone from AIRS are more-or-less similar to the distributions those from
406 ozonesonde. Here, the ozone variations are reflecting in terms of spatial as well as vertical
407 distributions. The bias and coefficient of determination (r^2) between ozonesonde and AIRS ozone
408 are studied along the longitude and latitude (Figures [S3S4](#) and [S4S5](#)). Lower biases (lesser than
409 10%) and higher r^2 are seen in the lower and middle troposphere. The poor correlation (<0.4) and
410 larger biases of up to 28% are seen at certain longitudes that are associated with higher altitudes
411 (> 20 km). Around the balloon launch site (Nainital, 79.45° E) highest r^2 score of 0.98 and low
412 bias of 1.4% are observed, which remain higher (r^2) and lower (bias) up to 80° E (Figure [S3S4](#)).

413

414

415

416 **3.2 Ozone Soundings and AIRS Ozone Profiles**

417 Figure 5 shows the average monthly ozone profiles for collocated observations of ozonesonde and
418 AIRS, respectively, during seven-year periods. The ozonesonde convolved with AIRS averaging
419 kernels [ozonesonde (AK)] and AIRS a-priori are also compared. The value of percentage
420 difference between ozonesonde (AK) and AIRS ozone at 706, 617, 496, 103, 29, and 14 hPa
421 altitudes are shown in figure 5, and the zoomed variations in the lower tropospheric ozone (surface
422 to 200 hPa) are also presented in the insets. AIRS slightly ($\sim 10\%$) underestimates ozone in the
423 lower troposphere during most of the months, except the summer-monsoon (June-August), where
424 an overestimation of up to 20% is observed. In the middle troposphere, around 300 hPa, an

425 underestimation in the range of 1 - 17% is seen for all months with an approaching tendency of
426 ozonesonde (AK) towards the true ozonesonde profiles. However, near the tropopause region,
427 AIRS retrievals considerably overestimate ozone by up to 102%. The overestimation was
428 highest for the winter season (82 - 102%), followed by the spring, and autumn, while lowest for
429 the summer-monsoon season (10 - 27%). In the stratosphere, where the sensitivity of AIRS is
430 higher (Figure 2c), the ozonesonde and AIRS differences were relatively lesser. Additionally,
431 AIRS retrieval shows an underestimation of 5 - 21% in this altitude region.

432

433 As expected, the difference between ozonesonde and AIRS is significantly reduced (Table 1) after
434 applying the averaging kernel or accounting for the sensitivity difference. This reduction was more
435 notable for the summer monsoon period near the tropopause, where the difference reduced from
436 92% to 19%, providing an improvement of 72%. The improvement was as high as 100% on a
437 monthly basis. Additionally, relative difference profiles were also analyzed for individual
438 soundings as well for the different seasons (Figure [SSS6](#)). Higher differences of about 150%
439 between AIRS and ozonesonde ozone observations were seen in the upper troposphere and lower
440 stratospheric (UTLS) region. The higher difference during winter and spring between these
441 observations in the UTLS region could be due to recurring ozone transport via tropopause folding
442 over the observation site. Such events may remain undetected by AIRS due to lower vertical
443 resolution leading to the missing of some tropopause folding events at lower altitudes (Figure 3).
444 However, in the lower troposphere, larger differences between ozonesonde and AIRS during
445 summer-monsoon are seen, which are due to low ozone and frequent cloudy conditions leading to
446 poor retrieval. The arrival of cleaner oceanic air during the south-west monsoon (or summer
447 monsoon) brings ozone-poor air and frequent cloudy conditions over northern India that weakens

448 the photochemical ozone production (Naja et al., 2014; Sarangi et al., 2014). Moreover, in the
449 lower troposphere, the limited sensitivity of hyperspectral satellite instruments has a significant
450 contribution from the a-priori information, which is also observed for AIRS retrieval (Figure 5).

451
452 Figure 6 shows the yearly time series analysis of the average ozone mixing ratio at four defined
453 layers, characterizing the middle troposphere (600 - 300 hPa), the upper troposphere (300 - 100
454 hPa), lower stratosphere (100 - 50 hPa), and middle stratosphere (50 - 10 hPa) respectively. A
455 prominent seasonality was seen in the time series throughout the years, which is quite clear in the
456 upper troposphere (300 - 100 hPa). The ozone seasonality contrast reflects the influence of
457 summer-monsoon and winter seasons. The seasonality contrast is similar between AIRS and
458 ozonesonde measurements, while a reversal of ozone seasonality is observed in the middle
459 stratospheric region compared to other layers. The opposite seasonality of the middle stratospheric
460 region is primarily due to dominant circulations, variation of solar radiation and dynamics. Total
461 column water vapor is also shown in Figure 6 that shows a tendency of anti-correlation with ozone
462 in the 300 - 100 hPa region.

463
464 We have also estimated the monsoon index by the difference between zonal (U) wind (MERRA-
465 2 reanalysis data) at 850 hPa over the Arabian Sea (40° E - 80° E, 5°N - 15° N) and over the central
466 Indian landmass (70° E - 90° E, 20° N - 30° N) as done by Wang et al. (2001).

467 In general, the positive values of the monsoon index correspond to strong monsoons and negative
468 values correspond to weak monsoon periods (Wang et al., 2001). During the weak monsoon, there
469 is relatively drier air, lower cloud cover and higher surface temperature compared to the strong
470 monsoon period (Lu et al., 2018). We observed a tendency of lower annual average ozone (from

471 ozonesonde and AIRS measurements) during greater (positive) monsoon index and higher annual
472 average ozone during lower (negative) monsoon index. Lu et al. (2018) have shown an anti-
473 correlation (0.46) of tropospheric ozone with monsoon index over the Indian region. The years
474 2011, 2012, 2014, and 2015 are classified as weak monsoon years and relatively higher ozone is
475 seen during these years, whereas for the years 2013, 2016, and 2017, strong monsoon is observed,
476 and average yearly ozone was lesser during these years (Figure 6 bottom left). The relative
477 difference of AIRS ozone with ozonesonde in the upper tropospheric region also shows an anti-
478 correlation (Figure 6) of 0.17 with total column water vapor. Furthermore, the larger ozone
479 differences between AIRS and ozonesonde are associated with the lower water vapor (Figure
480 [S6S7](#)), which may be arising due to the influence of ozone-sensitive water vapor (WV) channels
481 in mid-Infra-red regions. Further, in the middle troposphere (600-300 hPa), a secondary ozone
482 peak in post-monsoon is observed, which is suggested to be influenced by the biomass burning
483 (Figure [S7S8](#)) over northern India that seems to be missing in the AIRS ozone.

484
485 In the middle troposphere (600 - 300 hPa) and lower stratosphere (100 - 50 hPa), AIRS retrievals
486 show higher differences with respect to ozonesondes, while a nominal difference is observed for
487 the middle troposphere and middle stratosphere (Figure [S6S7](#)). Furthermore, a systematic increase
488 in standard deviation is also seen with the altitude. The higher standard deviations in the upper
489 tropospheric and stratospheric regions are mainly due to higher ozone variability associated with
490 stratosphere-troposphere exchange (STE) processes over the Himalayan region (Naja et al., 2016;
491 Bhardwaj et al., 2018).

492

493 **3.3 Statistical Analysis of AIRS Ozone Profiles**

494 Error analysis of AIRS retrieved ozone over the Himalayan region is performed with spatio-
495 temporal collocated ozonesonde observations as a reference. The methodology to calculate the
496 root mean square error (RMSE), bias, and standard deviation (STD) is described in [supplementary](#)
497 section [1.2.3](#). W_2 weighting statistics are utilized due to abrupt changes in atmospheric ozone with
498 altitude. Here bias and STD between AIRS and ozonesonde are calculated at different RTA layers
499 from surface to 10 hPa. Figure 7 shows the average variation of bias and STD at different RTA
500 layers from surface to 10 hPa over this region. The mean biases between ozonesonde and MLS, a
501 high vertical resolution satellite instrument, are also shown in figure 7. In general, higher positive
502 biases (~65%) and STDs (~25%) in AIRS ozone retrieval are seen in the UTLS region, where
503 MLS agrees well with ozonesonde. In the lower and middle troposphere, the AIRS ozone retrieval
504 is negatively biased (0 - 25%), which increases gradually from the surface to higher altitudes (~
505 350 hPa). A negative bias was also seen in the stratosphere of about 15%. Similar to the biases,
506 STDs are also smaller in the lower troposphere and stratosphere, with values of nearly 15%. The
507 higher statistical errors in the upper troposphere and the lower stratospheric region could be due
508 to lower ozone partial pressure and frequent stratospheric to tropospheric transport events over the
509 Himalayas (Rawat et al., 2020, 2021), which introduces errors either after a mismatch of events in
510 AIRS coarser vertical resolution or due to complex topography. Additionally, the AIRS tropopause
511 frequency distribution shows less ability of AIRS to capture deep intrusion events (Figure 3).
512 Further, AIRS trace gas retrieval largely depends on successful temperature retrieval and uses
513 temperature retrieval as an input parameter (Maddy and Barnett, 2008). Hence, temperature
514 retrieval error could also propagate to ozone, and statistical error analysis of AIRS temperature
515 shows relatively higher biases (~ 2 K) in the upper tropospheric region (Figure [S8S9](#)).

516

517 The statistical error analysis was more-or-less similar for both true and smoothed ozonesonde
518 profiles. However, notable reduction in tropospheric bias and vertical shifts of errors were also
519 observed after applying the averaging kernel matrix to the true ozonesonde throughout the profile.
520 A shift of the error peak is seen from the lower stratosphere to the upper troposphere. This could
521 be due to the higher sensitivity of AIRS retrieval in the lower stratosphere, which would have
522 minimized the error at these particular altitudes. However, in the upper troposphere, higher
523 contribution of a-priories, as well as other factors (i.e., STE), might have resulted in larger biases
524 and errors.

525

526 The histogram of differences between AIRS and ozonesonde (AK) is also studied at four defined
527 layers (Figure [8S10](#)). AIRS mostly underestimated ozone with a mean bias of 2.374 ppbv, 9.293
528 ppbv, and 39.8 ppbv in 800 - 600 hPa, 600 - 300 hPa, and 100 - 50 hPa layers, respectively, while
529 in the upper troposphere (300 - 100 hPa) AIRS overestimated with a mean bias of 43.22 ppbv.
530 Furthermore, distributions of differences are skewed toward the negative values in the lower
531 stratosphere and towards positive values in the upper troposphere. A more symmetric distribution
532 over the negative axis is observed in the middle and lower troposphere. We also studied the
533 correlation profiles for different seasons (Figure [8S10](#), right panel). A strong correlation is seen in
534 the lower and middle troposphere for spring and summer, while there is a poor correlation for
535 winter and autumn. In the lower troposphere, a larger difference between AIRS and ozonesonde
536 (AK) is observed, particularly during summer, with a relatively higher correlation mostly due to
537 the greater concurrence of AIRS a-priori with ozonesonde (AK). Whereas, in the upper
538 troposphere (300 - 100 hPa), a larger difference during winter and spring is primarily due to
539 frequent subtropical dynamics, while a higher correlation during the winter is mainly contributed

540 from the AIRS retrieval. Furthermore, analysis of the correlation coefficient between AIRS and
541 ozonesonde over different regions shows a higher correlation in the middle stratosphere (0.95) and
542 lower stratosphere (0.92), followed by upper troposphere (0.68), lower troposphere (0.62), and
543 middle troposphere (0.47).

544

545 **3.4 Assessment of AIRS Retrieval Algorithm with IASI and CrIS Radiance**

546 The MetOp/IASI and Soumi-NPP/CrIS radiance-based ozone products are assessed using
547 ozonesonde data over the central Himalayan region for one year (April 2014 to April 2015),
548 utilizing a total of 32 soundings. Here, the IASI and CrIS based ozone retrievals are research
549 products provided by NOAA, whose retrieval is based on the AIRS retrieval algorithm and follows
550 a similar averaging kernels matrix (Nalli et al., 2017). For IASI, due to the 09:30 ascending nodes
551 (morning overpass in India), ± 6 h loose temporal collocation is used. However, CrIS and AIRS
552 follow the same collocation due to a similar noontime overpass. The IASI, CrIS, and AIRS sensors
553 have 8461, 1305, and 2378 IR channels, respectively. Hence, analyzing their satellite ozone
554 products further helps to assess the AIRS retrieval algorithm for different IR radiances and channel
555 sets.

556

557 Figure [9a8a](#) shows the seasonal ozone profiles obtained from three IR satellite sensors along with
558 ozonesonde for one year period. All sensors showed more-or-less similar ozone peak altitude and
559 ozone gradient. The estimated ozone peak altitude for ozonesonde, AIRS, IASI, and CrIS are 11.35
560 hPa, 10 hPa, 9.11 hPa, and 7.78 hPa, respectively. The estimated average ozone gradient in regions
561 between tropopause to gradient peak are 231.5 ppbv/hPa, 199.0 ppbv/hPa, 193.2 ppbv/hPa, and
562 199.1 ppbv/hPa for ozonesonde, AIRS, CrIS, and IASI, respectively.

563

564 Moreover, the higher ozone values during spring throughout the troposphere are captured well by
565 all satellite sensors. Higher ozone during spring and winter in the UTLS region is observed well
566 by AIRS and IASI, similar to ozonesonde but such features seem to be missing in CrIS ozone
567 retrieval. At the same time, CrIS sensitivity looks relatively low, where the possible role of the
568 number of channels can be seen. However, IASI and AIRS have effectively captured the ozone
569 seasonal variability.

570

571 Figure 9b8b shows the weighted statistical error analysis of IASI, CrIS, and AIRS ozone retrieval
572 with the true ozonesonde observations. Here, the difference in sensitivity of the two data sets is
573 not accounted for as this section's primary aim is to assess the AIRS retrieved algorithm using
574 different IR sensor radiances and channel sets. All three space-borne sensors overestimated UTLS
575 ozone by more than 50%, however, in the stratosphere and lower troposphere, the bias was slightly
576 lower, and it is somewhat underestimated. Similar to bias, the STDs were also higher in the UTLS
577 region by more than 60%. A consistent larger differences in the UTLS region for all three IR
578 satellite sensors that share the similar radiative transfer model and retrieval algorithm shows the
579 possible influence of complex topography and the various STE processes, in introducing errors in
580 retrieval processes, apart from input a-priories of the retrieval.

581

582 Additionally, Pearson correlations between ozonesonde and IASI, CrIS, and AIRS are also studied
583 at five atmospheric layers (i.e., 600 - 800 hPa, 300 - 600 hPa, 100 - 300 hPa, 50 -100 hPa, and 10
584 - 50 hPa) (Table 2). A relatively stronger positive correlation is found in the middle stratosphere
585 (50 - 100 hPa) and lower stratosphere (50 - 100 hPa), which was highest for AIRS, followed by

586 CrIS and IASI, and a relatively low correlation is observed in the middle troposphere (300 - 600
587 hPa) for AIRS and IASI (~ 44% and 31%), while CrIS shows the poorest correlation in the lower
588 troposphere about 9%. The lower concurrence between ozonesonde and the satellite sensors in the
589 lower troposphere could be due to lower sensitivity and shorter lifetime of near-surface ozone that
590 could increase the a-priori contribution and sampling mismatch, respectively.

591

592 **3.5 Columnar Ozone**

593 **3.5.1 Total Column Ozone (TCO)**

594 Figure ~~10a9a~~ shows variations in monthly average total column ozone (TCO) from ozonesonde,
595 AIRS, and OMI during 2011 - 2017. Here the box plots are also overlaid on the mean column to
596 describe the distribution of monthly column data. In general, the TCO is higher during spring,
597 which subsequently drops in summer-monsoon. AIRS TCO shows a bimodal monthly variation
598 which is not seen in the ozonesonde and OMI observations, otherwise, its monthly variation is in
599 reasonable agreement with ozonesonde. The OMI TCO is in a good match with the ozonesonde
600 with a maximum difference of up to about 5 DU. Table 3 shows the difference in the TCO between
601 AIRS, OMI, and ozonesonde. AIRS shows considerable overestimation in the range of 2.2 - 22
602 DU for some months while notable underestimation (1.8 - 4 DU) for others, with respect to both
603 ozonesonde and OMI. The correlation between AIRS TCO and ozonesonde TCO is found to be
604 0.5 (Table S4). To further understand the cause of bimodal variations in AIRS (higher ozone during
605 August, September, and October), the AIRS ozone profiles were integrated between different
606 stratospheric regions (100 - 70 hPa, 70 - 50 hPa, 50 - 20 hPa, and 20 - 1 hPa) and we found that
607 the elevated total ozone during post-monsoon is mainly contributed from the altitude above 50
608 hPa.

609

610 **3.5.2 UTLS Ozone Column**

611 Figure ~~10b9b~~ shows the variations in the monthly average UTLS ozone column for collocated and
612 concurrent observations of AIRS, MLS, and ozonesonde during 2011 - 2017. The UTLS region
613 extends between 400 hPa to 70 hPa (Bian et al., 2007) for ozonesonde and AIRS, while for MLS,
614 the region between 261 hPa to 70 hPa is utilized. The recommended pressure levels for MLS v4
615 ozone retrieval are above 261 hPa (Livesey et al., 2013; Schwartz et al., 2015). In contrast to TCO,
616 higher ozone in UTLS is seen during the winter and spring (~ 45 DU) when there are recurring
617 downward transport events, while a clear drop of the column during the summer-monsoon shows
618 the convective transport of cleaner oceanic air to the higher altitudes. All the collocated
619 observations are able to capture the monthly variation effectively. However, there is a substantial
620 overestimation by more than 3 DU (Table S5) for all the months in AIRS measurements and MLS
621 mostly underestimate it, except during winter due to smaller integrated columns. Furthermore, the
622 larger whiskers of the box plot during winter and spring show the larger variations of the ozone in
623 the UTLS region. Though there were notable overestimations compared to ozonesonde, still UTLS
624 monthly variations are captured well by AIRS with a correlation of up to 75% (Table S4). In
625 addition, the correlation of ozonesonde and AIRS ozone at each pressure level in the UTLS region
626 is 0.81, which further increases with ozonesonde (AK) (of about 0.94). The persistent biases in the
627 satellite retrievals arises due to inadequate input parameters that can be improved by using more
628 accurate initial parameters and surface emissivity (Dufour et al., 2012; Boynard et al., 2018).

629

630 **3.5.3 Tropospheric Ozone Column**

631 Figure 10e9c shows the variations in the monthly average tropospheric ozone column utilizing
632 various collocated data sets during 2011 - 2017. The tropospheric ozone column is calculated by
633 integrating ozone profiles from the surface to the tropopause. WMO-defined lapse rate calculation
634 method is used to calculate tropopause height from balloon-borne and AIRS observations (Figure
635 3). Higher tropospheric ozone is observed during the spring and early summer (> 45 DU) when
636 annual crop-residue burning (Figure S7S8) events occur over northern India, apart from downward
637 transport from the stratosphere. A few cases of downward transport are discussed in the next
638 section. The tropospheric ozone column drops rapidly during the summer-monsoon when pristine
639 marine air reaches Nainital. A slight increase of column is also seen during the autumn, which is
640 again influenced by post-monsoon crop residue burning practices (Figure S7S8) over northern
641 India (Bhardwaj et al., 2016). The AIRS is able to capture the monthly variations very effectively;
642 however, there are larger biases. The biases with ozonesonde are higher when the tropopause is
643 taken from the balloon-borne observation, while with AIRS provided tropopause, the biases are
644 lesser or mostly within the one sigma limit. The correlation between ozonesonde and AIRS, when
645 used AIRS tropopause, is very strong (0.72). Like AIRS, the OMI/MLS column is in good
646 agreement and able to produce monthly variations; however, there are larger differences during
647 winter and spring of more than 10 DU. The tropospheric ozone column from ozonesonde is
648 different for balloon-borne LRT and AIRS tropopause, which could be due to the lower vertical
649 resolution of AIRS. AIRS calculates tropopause with an uncertainty of 1-2 km (Divakarla et al.,
650 2006). It can also be seen that on average a lower (about 28%) tropopause pressure (or higher
651 altitude) is calculated by AIRS compare to ozonesonde measurements (Figure 3).

652

653 **3.6 Case Studies of Biomass Burning and Downward Transport**

654 Over northern India, extensive agriculture practices and forest fires influence ozone at the surface
655 and higher altitudes (Kumar et al., 2011; Cristofanelli et al., 2014; Bhardwaj et al., 2016; Bhardwaj
656 et al., 2018). Based on MODIS fire counts, the days in between 1 March to 15 April over northern
657 India are classified as the low fire periods (LFP) as considered in previous studies over this region.
658 The high fire period (HFP) is classified when the fire counts over the observational site are more
659 than the median fire counts in the biomass burning period, typically from mid-April to May
660 (Bhardwaj et al., 2016). A total of 32 soundings (mid-April to May) are classified as HFP and 33
661 soundings (March to mid-April) are classified as LFP. Figure 4410 (left) shows the average ozone
662 profiles up to 6 km from ozonesonde and AIRS observations during HFP and LFP. The
663 ozonesonde data show enhancement in ozone by about 5 ppbv to about 11 ppbv during HFP as
664 compared to LFP that is accounting for a 5 - 20% increase. It is important to mention that
665 enhancement is greater in higher altitude regions that drop gradually above 400 hPa. The
666 enhancement is slightly lower (10 - 15%) in the AIRS profile, where most of it is contributed by
667 the a-priori profile (Figure S8S11).

668
669 Deep stratospheric intrusion or the downward transport (DT) of ozone-rich air from the
670 stratosphere to the troposphere significantly influences ozone profiles over the subtropical regions
671 (~~Collins, et al., 2003~~; Zhu, et al., 2006; Lal et al., 2014). Over the subtropical Himalayas, such
672 ozone intrusions are observed during the winter and spring seasons (Zhu et al., 2006; Ojha et al.,
673 2014). The DT events are classified based on the higher ozone in middle - upper troposphere seen
674 from ozonesonde with relatively larger Ertel potential vorticity (EPV) and lower humidity in
675 MERRA-2 reanalysis data. Based on this, 10 soundings (between January and mid-April) are
676 classified as DT events for ozonesonde and AIRS. Figure 4410 (right) shows ozone profiles from

677 ozonesonde (AK) and AIRS observations for high ozone DT events as well as the average ozone
678 profiles of corresponding months excluding the DT event. Though there are persistent positive
679 biases in AIRS ozone profile compared to ozonesonde in the middle/upper troposphere, still both
680 the observations have captured the influence of the downward transport on the ozone profile very
681 effectively and show an increase in the ozone of 10 - 20% in altitude range 2 - 16 km. Ozonesonde
682 based observations have shown about twofold increase in upper-middle tropospheric ozone due to
683 downward ozone transport over this region (Ojha et al., 2014). Further, the first guess profile's
684 contribution to AIRS retrieval during DTs is negligible (Figure [S9S11](#)) and shows the main
685 contribution from the AIRS observations itself. So, despite the persistent biases in the AIRS and
686 ozonesonde observations, AIRS is able to capture the influences of downward transport (DT) on
687 ozone profile notably well.

688

689

690

691

692 **3.7 Ozone Radiative Forcing**

693 Radiative forcing is a valuable metric to estimate the radiative impacts of any anthropogenic or
694 natural activity on the climate system (Ramaswamy et al., 2001). It measures the net radiation at
695 the surface, tropopause, and the top of the atmosphere due to any atmospheric constituents. Here
696 we discuss the ozone radiative forcing (RF) at the surface in the ultraviolet (UV) spectral range
697 (Antón et al., 2014; Mateos et al., 2020) using the ozonesonde, OMI, and AIRS total column ozone
698 (TCO) data. The RF is calculated based on Antón et al. (2014), relative to 1979 utilizing TOMS
699 TOC data in 1979, monthly averaged solar zenith angles of site, clearness index ~~based on~~

700 (~~Chakraborty et al., (2014)~~ and ~~Hawas et al., (1984), references therein~~) and respective monthly
701 average TCO data of AIRS, OMI, and ozonesonde. Rather than quantifying the RF values here,
702 our primary focus is to show how the discrepancies of satellite ozone data (mainly AIRS) can
703 impact the calculation of RF values. Figure ~~12~~11 shows the seasonal average ozone radiative
704 forcing (RF) relative to 1979. The annual average ozone RF during 2011 - 2017 is 4.86, 4.04, and
705 2.96 mWm^{-2} for ozonesonde, OMI, and AIRS, respectively. The RF values for ozonesonde and
706 OMI are comparable to Mateos et al. (2020) (4 mWm^{-2}) for the extratropical region. However, for
707 AIRS, the RF value is lower by 45%. Further, the seasonal average ozone RF (2011-2017) is
708 consistent between ozonesonde and OMI, while notable differences are seen in AIRS except
709 during the winter season when differences are marginal (Figure ~~12~~11). Also, it is noted (Table 3)
710 that the higher total ozone bias during autumn (as high as 22 DU) contributes to higher RF
711 differences in autumn (Figure ~~12~~11).

712

713

714

715

716 **4. Summary and Conclusions**

717 This study has utilized 242 ECC (EN-SCI) ozone soundings (during 2011 - 2017) conducted over
718 the Himalayan station (Nainital) to evaluate the AIRS version 6 ozone product and study the
719 performance during biomass burning events, ozone downward transport events and estimation of
720 ozone radiative forcing. AIRS ozone retrieval is evaluated in terms of retrieval sensitivity, retrieval
721 biases, retrieval errors, and ability to retrieve the natural variability of columnar ozone at different
722 altitude regions. This study is the first of its kind in the Himalayan region- and fills the void of

723 proper validation of various satellite ozone retrievals, particularly AIRS, over this complex terrain.

724 The AIRS averaging kernels information ~~wasis~~ applied to ozonesonde for a like-for-like
725 comparison to overcome their sensitivity differences. The monthly profile evaluation shows ozone
726 peak and ozone altitude dependency is captured well by AIRS retrieval with smaller but notable
727 underestimation (5 - 20%) in the lower-middle troposphere and stratosphere, while overestimation
728 in the UTLS region as high as 102%. We show a relatively higher sensitivity of AIRS ozone for
729 the summer monsoon in the UTLS region, where the biases between AIRS and ozonesonde
730 reduced from 92% to 19% after applying AIRS averaging kernel information.

731 Furthermore, the weighted statistical error analysis of AIRS retrieved ozone profiles with
732 ozonesonde shows higher positive biases (65%) and STD (25%) in the upper troposphere-, where
733 a high resolution satellite MLS agrees well with ozonesonde. While in the lower-middle
734 troposphere and stratosphere, AIRS ozone was negatively biased ~~ofby~~ less than 20%. In addition,
735 though the biases and errors are higher in the upper troposphere, there is a larger correlation of
736 about 81%, demonstrating the reasonable capability of AIRS to retrieve upper tropospheric ozone
737 variability with certain positive biases. Such biases in satellite retrieval can be eliminated by
738 choosing better emissivity inputs or other retrieval parameters.

739

740 The histogram of differences between AIRS and ozonesonde (AK) ~~demonstrated that AIRS~~ mostly
741 underestimated-shows an underestimation of AIRS ozone (2.374 - 39.8 ppbv), ~~while~~ except in the
742 upper troposphere, where a notable overestimation with a mean bias of about 43 ppbv is ~~seen in~~
743 the upper troposphere ~~observed~~. The AIRS ozone retrieval algorithm was further evaluated using

744 the radiance of IASI and CrIS sensors; these sensors provided similar error statistics as seen for
745 AIRS, with higher positive biases in the UTLS region.

746 The AIRS-derived columnar ozone amounts (i.e., total, UTLS, and tropospheric ozone) are also
747 evaluated to see whether the ozone variability at different altitude regions is being retrieved
748 correctly. The UTLS and tropospheric ozone monthly variations are captured well by AIRS with
749 persistent positive biases. However, the total ozone column shows bimodal monthly variations,
750 which was not evident in the ozonesonde and OMI total ozone observations. Further, we found a
751 higher total ozone column in AIRS during autumn, which is mostly coming from the stratospheric
752 region above 50 hPa. Furthermore, the capabilities of AIRS ozone retrieval to capture various
753 biomass burning and downward transport events have also been studied using fire counts and EPV
754 tracers. AIRS captures reasonable enhancements in ozone profiles (5 - 20%) after such events with
755 notable contributions of the a-priori, particularly in biomass-burning events.

756 Unlike the well-mixed greenhouse gases, the ozone radiative forcing (RF) remains uncertain due
757 to inadequate budget estimates and complex chemical processes. Stevenson et al. (2013) have
758 shown that a few percent uncertainties in ozone concentrations can produce a spread of ~17% in
759 ozone RF estimations. The total ozone discrepancies of AIRS lead to show lower RF (by about
760 45%) compared to ozonesonde and OMI and higher uncertainty in this Himalayan region. Here,
761 the role of in-situ observations from ozone soundings is shown to be important in improving the
762 satellite-retrieved ozone over the Himalayan region by assessing and providing insights upon its
763 errors and biases. This information over the Himalayan region could be applied to the ozone
764 retrieval from other satellite data sets, having long-term coverage. ~~This will~~ Such an evaluation
765 study is crucial for reducing biases in satellite retrieval and assessing the credibility of various
766 space-based ozone retrieval over the Himalayan region. It will also help better understand regional

767 ozone and radiation budgets over this Himalayan region and ~~offer an opportunity to~~
768 ~~understand~~perceive the possible differences between satellites and truth observations.

769

770 **Acknowledgments**

771 We are grateful to Director ARIES and ISRO-ATCTM project for supporting this work. Help from
772 Deepak and Nitin in balloon launches and coordination with the air traffic control is highly
773 acknowledged. The National Center for Atmospheric Research is sponsored by the National
774 Science Foundation. SL is grateful to INSA, New Delhi for the position and Director PRL,
775 Ahmedabad for the support. We highly acknowledge NOAA and NASA-EARTHDATA online
776 data portals for providing IASI, AIRS, and CrIS level2 data. We thank the NASA Goddard Space
777 Flight Center Ozone Processing Team for providing the OMI/MLS tropospheric ozone, OMI total
778 ozone column and JPL for MLS ozone profile. We would also like to acknowledge the use of the
779 MODIS fire data through FIRMS archive download. Use of map from Google earth is also
780 acknowledged. We thank the reviewers for their constructive comments and valuable suggestions.

781

782 **Data availability:** Satellite data are available in the respective web portal. Ozone sonde data could
783 be made available on a reasonable request by writing to the corresponding author.

784

785

786

787 **References**

788 Antón, M., D. Mateos, R. Román, A. Valenzuela, L. Alados-Arboledas, and F. J. Olmo.: A method
789 to determine the ozone radiative forcing in the ultra-violet range from experimental data, *J.*
790 *Geophys. Res. Atmos.*, 119, 1860–1873, doi:10.1002/2013JD020444, 2014.

791

792 Aghedo, A.M., Bowman, K.W., Worden, H.M., Kulawik, S.S., Shindell, D.T., Lamarque, J.F.,
793 Faluvegi, G., Parrington, M., Jones, D.B.A. and Rast, S.: The vertical distribution of ozone
794 instantaneous radiative forcing from satellite and chemistry climate models. *Journal of*
795 *Geophysical Research: Atmospheres*, 116(D1), 2011.

796

797 Bai, W., Wu, C., Li, J. and Wang, W.: Impact of terrain altitude and cloud height on ozone remote
798 sensing from satellite, *Journal of Atmospheric and Oceanic Technology*, 31(4), pp.903-912, 2014.

799

800 Barre, J., Peuch, V.H., Attié, J.L., Amraoui, L.E., Lahoz, W.A., Josse, B., Claeysman, M. and
801 Nedelec, P.: Stratosphere-troposphere ozone exchange from high resolution MLS ozone analyses,
802 *Atmos. Chem. Phys.*, 12(14), pp.6129-6144, 2012.

803

804 Bhardwaj, P., Naja, M., Kumar, R. and Chandola, H.C.: Seasonal, interannual, and long-term
805 variabilities in biomass burning activity over South Asia, *Environmental Science and Pollution*
806 *Research*, 23(5), pp.4397-4410, 2016.

807

808 Bhardwaj, P., Naja, M., Rupakheti, M., Lupascu, A., Mues, A., Panday, A. K., Kumar, R., Mahata,
809 K. S., Lal, S., Chandola, H. C., and Lawrence, M. G.: Variations in surface ozone and carbon
810 monoxide in the Kathmandu Valley and surrounding broader regions during SusKat-ABC field

811 campaign: role of local and regional sources, *Atmos. Chem. Phys.*, 18, 11949–11971,
812 <https://doi.org/10.5194/acp-18-11949-2018>, 2018.

813

814 Bhartia, P.K., McPeters, R.D., Mateer, C.L., Flynn, L.E. and Wellemeyer, C.: Algorithm for the
815 estimation of vertical ozone profiles from the backscattered ultraviolet technique, *J. Geophys. Res.*
816 *Atmos.*, 101(D13), pp.18793-18806, 1996.

817

818 Bian, J., Gettelman, A., Chen, H. and Pan, L.L.: Validation of satellite ozone profile retrievals
819 using Beijing ozonesonde data, *J. Geophys. Res. Atmos.*, 112(D6), 2007.

820

821 Boynard, A., Hurtmans, D., Koukouli, M.E., Goutail, F., Bureau, J., Safieddine, S., Lerot, C.,
822 Hadji-Lazaro, J., Wespes, C., Pommereau, J.P. and Pazmino, A.: Seven years of IASI ozone
823 retrievals from FORLI: validation with independent total column and vertical profile
824 measurements, *Atmos. Meas. Tech.*, 9(9), pp.4327-4353, 2016.

825

826 Boynard, A., Hurtmans, D., Garane, K., Goutail, F., Hadji-Lazaro, J., Koukouli, M. E., Wespes,
827 C., Vigouroux, C., Keppens, A., Pommereau, J.-P., Pazmino, A., Balis, D., Loyola, D., Valks, P.,
828 Sussmann, R., Smale, D., Coheur, P.-F., and Clerbaux, C.: Validation of the IASI
829 FORLI/EUMETSAT ozone products using satellite (GOME-2), ground-based (Brewer–Dobson,
830 SAOZ, FTIR) and ozonesonde measurements, *Atmos. Meas. Tech.*, 11, 5125–5152,
831 <https://doi.org/10.5194/amt-11-5125-2018>, 2018.

832

833 Brunamonti-S. et al., S., Jorge, T., Oelsner, P., Hanumanthu, S., Singh, B. B., Kumar, K. R.,
834 Sonbawne, S., Meier, S., Singh, D., Wienhold, F. G., Luo, B. P., Boettcher, M., Poltera, Y.,
835 Jauhiainen, H., Kayastha, R., Karmacharya, J., Dirksen, R., Naja, M., Rex, M., Fadnavis, S., and
836 Peter, T.: Balloon-borne measurements of temperature, water vapor, ozone and aerosol backscatter
837 on the southern slopes of the Himalayas during StratoClim 2016–2017, Atmos. Chem. Phys., 18,
838 15937–15957, <https://doi.org/10.5194/acp-18-15937-2018>, —2018:[https://doi.org/10.5194/acp-18-](https://doi.org/10.5194/acp-18-15937-2018)
839 [15937-2018](https://doi.org/10.5194/acp-18-15937-2018), 2018.

840

841 Cazorla, M. and Herrera, E. An ozonesonde evaluation of spaceborne observations in the Andean
842 tropics. Scientific reports, 12(1), pp.1-8, 2022.

843

844 Chakraborty, S., Sadhu, P.K. and Nitai, P.A.L.: New location selection criterions for solar PV
845 power plant. International Journal of Renewable Energy Research, 4(4), pp.1020-1030, 2014.

846

847 Clerbaux, C., Hadji-Lazaro, J., Turquety, S., George, M., Coheur, P.F., Hurtmans, D., Wespes, C.,
848 Herbin, H., Blumstein, D., Tourniers, B. and Phulpin, T.: The IASI/MetOp1 Mission: First
849 observations and highlights of its potential contribution to GMES2, Space Research Today, 168,
850 pp.19-24, 2007.

851

852 Coheur, P.F., Barret, B., Turquety, S., Hurtmans, D., Hadji-Lazaro, J. and Clerbaux, C.: Retrieval
853 and characterization of ozone vertical profiles from a thermal infrared nadir sounder, J. Geophys.
854 Res. Atmos., 110(D24), 2005.

855

856 ~~Collins, W. J., R. G. Derwent, B. Garnier, C. E. Johnson, M. G. Sanderson, and D. S. Stevenson.:
857 Effect of stratosphere-troposphere exchange on the future tropospheric ozone trend, J. Geophys.
858 Res., 108(D12), 8528, doi:10.1029/2002JD002617, 2003.~~

859

860 Cristofanelli, P., Putero, D., Adhikary, B., Landi, T.C., Marinoni, A., Duchi, R., Calzolari, F., Laj,
861 P., Stocchi, P., Verza, G. and Vuillermoz, E.: Transport of short-lived climate forcers/pollutants
862 (SLCF/P) to the Himalayas during the South Asian summer monsoon onset, Environmental
863 Research Letters, 9(8), p.084005, 2014.

864

865 Divakarla, M., Barnet, C., Goldberg, M., Maddy, E., Wolf, W., Flynn, L., Xiong, X., Wei, J., Zhou,
866 L. and Liu, X.: Validation of Atmospheric Infrared Sounder (AIRS) temperature, water vapor, and
867 ozone retrievals with matched radiosonde and ozonesonde measurements and forecasts, In
868 Multispectral, Hyperspectral, and Ultraspectral Remote Sensing Technology, Techniques, and
869 Applications, International Society for Optics and Photonics, Vol. 6405, p. 640503, 2006.

870

871 Divakarla, M., Barnet, C., Goldberg, M., Maddy, E., Irion, F., Newchurch, M., Liu, X., Wolf, W.,
872 Flynn, L., Labow, G. and Xiong, X.: Evaluation of Atmospheric Infrared Sounder ozone profiles
873 and total ozone retrievals with matched ozonesonde measurements, ECMWF ozone data, and
874 Ozone Monitoring Instrument retrievals, J. Geophys. Res. Atmos., 113(D15), 2008.

875

876 Dufour, G., Eremenko, M., Griesfeller, A., Barret, B., LeFlochmoën, E., Clerbaux, C., Hadji-
877 Lazaro, J., Coheur, P.F. and Hurtmans, D.: Validation of three different scientific ozone products
878 retrieved from IASI spectra using ozonesondes, Atmos. Meas. Tech., 5(3), pp.611-630, 2012.

879

880 Ebi, K.L. and McGregor, G., Climate change, tropospheric ozone and particulate matter, and health
881 impacts, Environmental health perspectives, 116(11), pp.1449-1455, 2008.

882

883 Fadnavis, S., Dhomse, S., Ghude, S., Iyer, U., Buchunde, P., Sonbawne, S. and Raj, P.E.: Ozone
884 trends in the vertical structure of Upper Troposphere and Lower stratosphere over the Indian
885 monsoon region, International Journal of Environmental Science and Technology, 11(2), pp.529-
886 542, 2014.

887

888 ~~Finlayson Pitts, B.J. and Pitts, J.N.: Tropospheric air pollution: ozone, airborne toxics, polycyclic
889 aromatic hydrocarbons, and particles, Science, 276(5315), pp.1045-1051, 1997.~~

890

891 Fishbein, E., Farmer, C.B., Granger, S.L., Gregorich, D.T., Gunson, M.R., Hannon, S.E.,
892 Hofstadter, M.D., Lee, S.Y., Leroy, S.S. and Strow, L.L.: Formulation and validation of simulated
893 data for the Atmospheric Infrared Sounder (AIRS), IEEE Transactions on Geoscience and Remote
894 Sensing, 41(2), pp.314-329, 2003.

895

896 Fishman, J., Ramanathan, V., Crutzen, P.J. and Liu, S.C.: Tropospheric ozone and climate, Nature,
897 282(5741), pp.818-820, 1979.

898

899 ~~Fishman, J., Minnis, P. and Reichle Jr, H.G.: Use of satellite data to study tropospheric ozone in
900 the tropics, J. Geophys. Res. Atmos., 91(D13), pp.14451-14465, 1986.~~

901

902 ~~Fishman, J.~~ and Larsen, J.C.: Distribution of total ozone and stratospheric ozone in the tropics:
903 Implications for the distribution of tropospheric ozone, J. Geophys. Res. Atmos., 92(D6), pp.6627-
904 6634, 1987.

905
906 Foret, G., Eremenko, M., Cuesta, J., Sellitto, P., Barré, J., Gaubert, B., Coman, A., Dufour, G.,
907 Liu, X., Joly, M. and Doche, C.: Ozone pollution: What can we see from space? A case study, J.
908 Geophys. Res. Atmos., 119(13), pp.8476-8499, 2014.

909
910 Forster, P.M., Bodeker, G., Schofield, R., Solomon, S. and Thompson, D.: Effects of ozone cooling
911 in the tropical lower stratosphere and upper troposphere, Geophysical Research Letters, 34(23),
912 2007.

913
914 ~~Fry, M.M., Naik, V., West, J.J., Schwarzkopf, M.D., Fiore, A.M., Collins, W.J., Dentener, F.J.,~~
915 ~~Shindell, D.T., Atherton, C., Bergmann, D. and Duncan, B.N.: The influence of ozone precursor~~
916 ~~emissions from four world regions on tropospheric composition and radiative climate forcing.~~
917 ~~Journal of Geophysical Research: Atmospheres, 117(D7), 2012.~~

918
919 Gauss, M., Myhre, G., Pitari, G., Prather, M.J., Isaksen, I.S.A., Berntsen, T.K., Brasseur, G.P.,
920 Dentener, F.J., Derwent, R.G., Hauglustaine, D.A. and Horowitz, L.W.: Radiative forcing in the
921 21st century due to ozone changes in the troposphere and the lower stratosphere, J. Geophys. Res.
922 Atmos., 108(D9), 2003.

923

924 Hauglustaine, D.A. and Brasseur, G.P.: Evolution of tropospheric ozone under anthropogenic
925 activities and associated radiative forcing of climate, J. Geophys. Res. Atmos., 106(D23),
926 pp.32337-32360, 2001.

927

928 ~~Hawas, M.M. and Muneer, T.; Study of diffuse and global radiation characteristics in~~
929 ~~India. Energy Conversion and Management, 24(2), pp.143-149, 1984.~~

930

931 Hudson, R.D. and Thompson, A.M.: Tropical tropospheric ozone from total ozone mapping
932 spectrometer by a modified residual method, J. Geophys. Res. Atmos., 103(D17), pp.22129-
933 22145, 1998.

934

935 Hegglin, M. I., Fahey, D. W., McFarland, M., Montzka, S. A., and Nash, E. R.: Twenty questions
936 and answers about the ozone layer: 2014 update, Scientific Assessment of Ozone Depletion: 2014,
937 84 pp., World Meteorological Organization, Geneva, Switzerland, ISBN 978-9966-076-02-1,
938 2015.

939

940 Irion, F.W., Kahn, B.H., Schreier, M.M., Fetzer, E.J., Fishbein, E., Fu, D., Kalmus, P., Wilson,
941 R.C., Wong, S. and Yue, Q.: Single-footprint retrievals of temperature, water vapor and cloud
942 properties from AIRS. Atmospheric Measurement Techniques, 11(2), pp.971-995, 2018.

943

944 Kim, J.H. and Newchurch, M.J.: Climatology and trends of tropospheric ozone over the eastern
945 Pacific Ocean: The influences of biomass burning and tropospheric dynamics, Geophysical
946 research letters, 23(25), pp.3723-3726, 1996.

947

948 Komhyr, W.D., Barnes, R.A., Brothers, G.B., Lathrop, J.A. and Opperman, D.P.: Electrochemical
949 concentration cell ozonesonde performance evaluation during STOIC 1989, *J. Geophys. Res.*
950 *Atmos.*, 100(D5), pp.9231-9244, 1995.

951

952 Komhyr, W.D.: Nonreactive gas sampling pump. *Review of Scientific Instruments*, 38(7), pp.981-
953 983, 1967.

954

955 Kumar, R., Naja, M., Satheesh, S.K., Ojha, N., Joshi, H., Sarangi, T., Pant, P., Dumka, U.C.,
956 Hegde, P. and Venkataramani, S.: Influences of the springtime northern Indian biomass burning
957 over the central Himalayas. *Journal of Geophysical Research: Atmospheres*, 116(D19), 2011.

958

959 Kumar, R., Naja, M., Pfister, G.G., Barth, M.C. and Brasseur, G.P.: Simulations over South Asia
960 using the Weather Research and Forecasting model with Chemistry (WRF-Chem): set-up and
961 meteorological evaluation, *Geoscientific Model Development*, 5(2), pp.321-343, 2012a.

962

963 Kumar, R., Naja, M., Pfister, G.G., Barth, M.C., Wiedinmyer, C. and Brasseur, G.P.: Simulations
964 over South Asia using the Weather Research and Forecasting model with Chemistry (WRF-
965 Chem): chemistry evaluation and initial results, *Geoscientific Model Development*, 5(3), pp.619-
966 648, 2012b.

967

968 Lacis, A.A., Wuebbles, D.J. and Logan, J.A.: Radiative forcing of climate by changes in the
969 vertical distribution of ozone, *J. Geophys. Res. Atmos.*, 95(D7), pp.9971-9981, 1990.

970

971 Lal S., S. Venkataramani, S. Srivastava, S. Gupta, M. Naja, T. Sarangi, X. Liu.: Transport effects
972 on the vertical distribution of tropospheric ozone over the tropical marine regions surrounding
973 India, *J. Geophys. Res.*,118, 1513-1524, doi:10.1002/jgrd.50180, 2013.

974

975 Lal S., S. Venkataramani, N. Chandra, O. R. Cooper, J. Brioude, and M. Naja, Transport effects
976 on the vertical distribution of tropospheric ozone over western India, *J. Geophys. Res. Atmos.*,
977 119, doi:10.1002/2014JD021854, 2014.

978

979 Lal, S., Venkataramani, S., Naja, M., Kuniyal, J.C., Mandal, T.K., Bhuyan, P.K., Kumari, K.M.,
980 Tripathi, S.N., Sarkar, U., Das, T. and Swamy, Y.V.: Loss of crop yields in India due to surface
981 ozone: An estimation based on a network of observations, *Environmental Science and Pollution*
982 *Research*, 24(26), pp.20972-20981, 2017.

983

984 Lawrence, M.G. and Lelieveld, J.: Atmospheric pollutant outflow from southern Asia: a review,
985 *Atmospheric Chemistry and Physics*, 10(22), pp.11017-11096, 2010.

986

987 Lelieveld, J., Haines, A. and Pozzer, A.: Age-dependent health risk from ambient air pollution: a
988 modelling and data analysis of childhood mortality in middle-income and low-income countries,
989 *The lancet Planetary health*, 2(7), pp.e292-e300, 2018.

990

991 Livesey, N.J., Logan, J.A., Santee, M.L., Waters, J.W., Doherty, R.M., Read, W.G., Froidevaux,
992 L. and Jiang, J.H.; Interrelated variations of O₃, CO and deep convection in the

993 tropical/subtropical upper troposphere observed by the Aura Microwave Limb Sounder (MLS)
994 during 2004–2011. Atmospheric Chemistry and Physics, 13(2), pp.579-598, 2013.
995

~~996 Logan, J.A.: Tropospheric ozone: Seasonal behavior, trends, and anthropogenic influence, J.~~
~~997 Geophys. Res. Atmos., 90(D6), pp.10463-10482, 1985.~~
998

999 Lu, X., Zhang, L., Liu, X., Gao, M., Zhao, Y. and Shao, J., 2018. Lower tropospheric ozone over
1000 India and its linkage to the South Asian monsoon. Atmospheric Chemistry and Physics, 18(5),
1001 pp.3101-3118.
1002

1003 Maddy, E.S. and Barnett, C.D.: Vertical resolution estimates in version 5 of AIRS operational
1004 retrievals, IEEE Transactions on Geoscience and Remote Sensing, 46(8), pp.2375-2384, 2008.
1005

1006 Mateos, D. and Antón, M.: Worldwide Evaluation of Ozone Radiative Forcing in the UV-B Range
1007 between 1979 and 2014. Remote Sensing, 12(3), p.436, 2020.
1008

~~1009 McPeters, R.D., Miles, T., Flynn, L.E., Wellemeyer, C.G. and Zawodny, J.M.: Comparison of~~
~~1010 SBUV and SAGE II ozone profiles: Implications for ozone trends, J. Geophys. Res. Atmos.,~~
~~1011 99(D10), pp.20513-20524, 1994.~~
1012

1013

1014 ~~McPeters, R.D.~~, Labow, G.J. and Logan, J.A.: Ozone climatological profiles for satellite retrieval
1015 algorithms, J. Geophys. Res. Atmos., 112(D5), 2007.

1016

1017 McPeters, R.D. and Labow, G.J.: Climatology 2011: An MLS and sonde derived ozone
1018 climatology for satellite retrieval algorithms. Journal of Geophysical Research:
1019 Atmospheres, 117(D10), 2012.

1020

1021 Monahan, K.P., Pan, L.L., McDonald, A.J., Bodeker, G.E., Wei, J., George, S.E., Barnett, C.D. and
1022 Maddy, E.: Validation of AIRS v4 ozone profiles in the UTLS using ozonesondes from Lauder,
1023 NZ and Boulder, USA, J. Geophys. Res. Atmos., 112(D17), 2007.

1024

1025 Monks, P.S., Archibald, A.T., Colette, A., Cooper, O., Coyle, M., Derwent, R., Fowler, D.,
1026 Granier, C., Law, K.S., Mills, G.E. and Stevenson, D.S.: Tropospheric ozone and its precursors
1027 from the urban to the global scale from air quality to short-lived climate forcer. Atmospheric
1028 Chemistry and Physics, 15(15), pp.8889-8973, 2015.

1029

1030 ~~Munro, R., Siddans, R., Reburn, W.J. and Kerridge, B. J.: Direct measurement of tropospheric~~
1031 ~~ozone distributions from space, Nature, 392(6672), pp.168-171, 1998.~~

1032

1033 1998.

1034

1035 Myhre, G., Aas, W., Cherian, R., Collins, W., Faluvegi, G., Flanner, M., Forster, P., Hodnebrog,
1036 Ø., Klimont, Z., Lund, M.T. and Mülmenstädt, J.: Multi-model simulations of aerosol and ozone
1037 radiative forcing due to anthropogenic emission changes during the period 1990–2015.
1038 Atmospheric Chemistry and Physics, 17(4), pp.2709-2720, 2017.

1039

1040 Naja, M., C Mallik, T. Sarangi, V Sheel, S. Lal, SO₂ measurements at a high altitude site in the
1041 central Himalayas: Role of regional transport, Atmospheric Environment,
1042 doi:10.1016/j.atmosenv.2014.08.031, 2014.

1043

1044 Naja M., Piyush Bhardwaj, N. Singh, Phani Kumar, R. Kumar, N. Ojha, Ram Sagar, S. K.
1045 Satheesh, K. Krishna Moorthy and V. R. Kotamarthi: High-frequency vertical profiling of
1046 meteorological parameters using AMF1 facility during RAWEX–GVAX at ARIES, Nainital,
1047 Current Science, vol 111, issue 1, 2016.

1048

1049 Nalli, N.R., Barnet, C.D., Reale, A., Tobin, D., Gambacorta, A., Maddy, E.S., Joseph, E., Sun, B.,
1050 Borg, L., Mollner, A.K. and Morris, V.R.: Validation of satellite sounder environmental data
1051 records: Application to the Cross-track Infrared Microwave Sounder Suite, J. Geophys. Res.
1052 Atmos., 118(24), pp.13-628, 2013.

1053

1054 Nalli, N.R., Gambacorta, A., Liu, Q., Tan, C., Iturbide-Sanchez, F., Barnet, C.D., Joseph, E.,
1055 Morris, V.R., Oyola, M. and Smith, J.W.: Validation of Atmospheric Profile Retrievals from the
1056 SNPP NOAA-Unique Combined Atmospheric Processing System. Part 2: Ozone, IEEE
1057 Transactions on Geoscience and Remote Sensing, 56(1), pp.598-607, 2017.

1058

1059 ~~Nassar, R., Logan, J.A., Worden, H.M., Megretskaja, I.A., Bowman, K.W., Osterman, G.B.,~~
1060 ~~Thompson, A.M., Tarasick, D.W., Austin, S., Claude, H. and Dubey, M.K. Validation of~~
1061 ~~Tropospheric Emission Spectrometer (TES) nadir ozone profiles using ozonesonde measurements.~~
1062 ~~Journal of Geophysical Research: Atmospheres, 113(D15), 2008.~~

1063

1064 Ojha, N., Naja, M., Sarangi, T., Kumar, R., Bhardwaj, P., Lal, S., Venkataramani, S., Sagar, R.,
1065 Kumar, A. and Chandola, H.C.: On the processes influencing the vertical distribution of ozone
1066 over the central Himalayas: Analysis of yearlong ozonesonde observations, *Atmospheric*
1067 *Environment*, 88, pp.201-211, 2014.

1068

1069 Pagano, T.S., Aumann, H.H., Hagan, D.E. and Overoye, K.: Prelaunch and in-flight radiometric
1070 calibration of the Atmospheric Infrared Sounder (AIRS), *IEEE transactions on geoscience and*
1071 *remote sensing*, 41(2), pp.265-273, 2003.

1072

1073 Pierce, R.B., Al-Saadi, J., Kittaka, C., Schaack, T., Lenzen, A., Bowman, K., Szykman, J., Soja,
1074 A., Ryerson, T., Thompson, A.M. and Bhartia, P.: Impacts of background ozone production on
1075 Houston and Dallas, Texas, air quality during the Second Texas Air Quality Study field mission,
1076 *J. Geophys. Res. Atmos.*, 114(D7), 2009.

1077

1078 Pittman, J.V., Pan, L.L., Wei, J.C., Irion, F.W., Liu, X., Maddy, E.S., Barnet, C.D., Chance, K.
1079 and Gao, R.S.: Evaluation of AIRS, IASI, and OMI ozone profile retrievals in the extratropical
1080 tropopause region using in situ aircraft measurements, *J. Geophys. Res. Atmos.*, 114(D24), 2009.

1081

1082 Ramaswamy, V., Boucher, O., Haigh, J., Hauglustaine, D., Haywood, J., Myhre, G., Nakajima,
1083 T., Shi, G.Y. and Solomon, S.: Radiative forcing of climate change. *Climate change 2001: the*
1084 *scientific basis. Contribution of working group I to the third assessment report of the*

1085 intergovernmental panel on climate change. DJ Griggs, M Noguer, PJ van der Linden, X Dai, K
1086 Maskell and CA Johnson (Cambridge: Cambridge University Press) pp, 350, p.416, 2001.
1087
1088 Rawat, P., Naja, M., Thapliyal, P.K., Srivastava, S., Bhardwaj, P., Kumar, R., Bhattacharjee, S.,
1089 Venkatramani, S., Tiwari, S.N. and Lal, S.: Assessment of vertical ozone profiles from INSAT-
1090 3D sounder over the Central Himalaya. *Current Science*, 119(7), p.1113, 2020.
1091
1092 Rawat, P. and Naja, M.: Remote sensing study of ozone, NO₂, and CO: some contrary effects of
1093 SARS-CoV-2 lockdown over India. *Environ Sci Pollut Res*, [https://doi.org/10.1007/s11356-021-](https://doi.org/10.1007/s11356-021-17441-2)
1094 [17441-2](https://doi.org/10.1007/s11356-021-17441-2), 2021.
1095
1096 Rodgers, C.D., 1976. Retrieval of atmospheric temperature and composition from remote
1097 measurements of thermal radiation. *Reviews of Geophysics*, 14(4), pp.609-624.
1098
1099 Rodgers, C.D., 1990. Characterization and error analysis of profiles retrieved from remote
1100 sounding measurements. *Journal of Geophysical Research: Atmospheres*, 95(D5), pp.5587-5595.
1101
1102 Rodgers, C.D. and Connor, B.J., 2003. Intercomparison of remote sounding instruments. *Journal*
1103 *of Geophysical Research: Atmospheres*, 108(D3).
1104
1105 Sarangi T., M. Naja, N. Ojha, R. Kumar, S. Lal, S. Venkataramani, A. Kumar, R. Sagar and H. C.
1106 Chandola: First simultaneous measurements of ozone, CO and NO_y at a high altitude regional

1107 representative site in the central Himalayas, *J. Geophys. Res.*, 119, doi:10.1002/2013JD020631,
1108 2014.

1109

1110 Schwartz, M., Froidevaux, L., Livesey, N. and Read, W.: MLS/Aura Level 2 Ozone (O₃) Mixing
1111 Ratio V004, Greenbelt, MD, USA, Goddard Earth Sciences Data and Information Services Center
1112 (GES DISC), 10.5067/Aura/MLS/DATA2017, 2015.

1113

1114 Shindell, D., Kuylenstierna, J.C., Vignati, E., van Dingenen, R., Amann, M., Klimont, Z.,
1115 Anenberg, S.C., Muller, N., Janssens-Maenhout, G., Raes, F. and Schwartz, J.: Simultaneously
1116 mitigating near-term climate change and improving human health and food security, *Science*,
1117 335(6065), pp.183-189, 2012.

1118

1119 Smit, H.G., Straeter, W., Johnson, B.J., Oltmans, S.J., Davies, J., Tarasick, D.W., Hoegger, B.,
1120 Stubi, R., Schmidlin, F.J., Northam, T. and Thompson, A.M.: Assessment of the performance of
1121 ECC-ozonesondes under quasi-flight conditions in the environmental simulation chamber:
1122 Insights from the Juelich Ozone Sonde Intercomparison Experiment (JOSIE), *Journal of*
1123 *Geophysical Research: Atmospheres*, 112(D19), 2007.

1124

1125 Smit, H. G. J., Thompson, A. M., & ASOPOS Panel. (2020). ASOPOS 2.0: Assessment of
1126 Standard Operating Procedures for Ozone Sondes, WMO/GAW Report.

1127

1128 Srivastava S., Manish Naja, V. Thouret: Influences of regional pollution and long range transport
1129 over Hyderabad using ozone data from MOZAIC, Atmospheric Environment, 117, pp.135-146,
1130 2015.
1131
1132 Stauffer, R.M., Thompson, A.M., Kollonige, D.E., Tarasick, D.W., Van Malderen, R., Smit, H.G.,
1133 Vömel, H., Morris, G.A., Johnson, B.J., Cullis, P.D. and Stübi, R.: An examination of the recent
1134 stability of ozonesonde global network data. Earth and Space Science, 9(10), p.e2022EA002459,
1135 2022.
1136
1137 Stevenson, D.S., Young, P.J., Naik, V., Lamarque, J.F., Shindell, D.T., Voulgarakis, A., Skeie,
1138 R.B., Dalsoren, S.B., Myhre, G., Berntsen, T.K. and Folberth, G.A.: Tropospheric ozone changes,
1139 radiative forcing and attribution to emissions in the Atmospheric Chemistry and Climate Model
1140 Intercomparison Project (ACCMIP), Atmos. Chem. Phys., 13(6), pp.3063-3085, 2013.
1141
1142 Susskind, J., Barnet, C.D. and Blaisdell, J.M.: Retrieval of atmospheric and surface parameters
1143 from AIRS/AMSU/HSB data in the presence of clouds, IEEE Transactions on Geoscience and
1144 Remote Sensing, 41(2), pp.390-409, 2003.
1145
1146 Susskind, J., Barnet, C., Blaisdell, J., Iredell, L., Keita, F., Kouvaris, L., Molnar, G. and Chahine,
1147 M.: Accuracy of geophysical parameters derived from Atmospheric Infrared Sounder/Advanced
1148 Microwave Sounding Unit as a function of fractional cloud cover, J. Geophys. Res. Atmos.,
1149 111(D9), 2006.
1150
1151 Tarasick, D., Galbally, I.E., Cooper, O.R., Schultz, M.G., Ancellet, G., Leblanc, T., Wallington,

1152 T.J., Ziemke, J., Liu, X., Steinbacher, M. and Staehelin, J.: Tropospheric Ozone Assessment
1153 Report: Tropospheric ozone from 1877 to 2016, observed levels, trends and uncertainties.
1154 *Elementa: Science of the Anthropocene*, 7, 2019.

1155

1156 Thornhill, G.D., Collins, W.J., Kramer, R.J., Olivié, D., Skeie, R.B., O'Connor, F.M., Abraham,
1157 N.L., Checa-Garcia, R., Bauer, S.E., Deushi, M. and Emmons, L.K.: Effective radiative forcing
1158 from emissions of reactive gases and aerosols—a multi-model comparison. *Atmospheric Chemistry
1159 and Physics*, 21(2), pp.853-874, 2021.

1160

1161 Veefkind, J.P., de Haan, J.F., Brinksma, E.J., Kroon, M. and Levelt, P.F.: Total ozone from the
1162 Ozone Monitoring Instrument (OMI) using the DOAS technique, *IEEE transactions on geoscience
1163 and remote sensing*, 44(5), pp.1239-1244, 2006.

1164

1165 Verstraeten, W. W., Boersma, K. F., Zörner, J., Allaart, M. A. F., Bowman, K. W., and Worden,
1166 J. R.: Validation of six years of TES tropospheric ozone retrievals with ozonesonde measurements:
1167 implications for spatial patterns and temporal stability in the bias, *Atmos. Meas. Tech.*, 6, 1413–
1168 1423, <https://doi.org/10.5194/amt-6-1413-2013>, 2013.

1169

1170 Wang, W.C., Zhuang, Y.C. and Bojkov, R.D.: Climate implications of observed changes in ozone
1171 vertical distributions at middle and high latitudes of the Northern Hemisphere, *Geophysical
1172 research letters*, 20(15), pp.1567-1570, 1993.

1173

1174 Wang, B., R. Wu, K.-M. Lau: Interannual variability of Asian summer monsoon: Contrast between
1175 the Indian and western North Pacific-East Asian monsoons. *J. Climate*, 14, 4073-4090, 2001.

1176

1177 Wang, H.R., Damadeo, R., Flittner, D., Kramarova, N., Taha, G., Davis, S., Thompson, A.M.,
1178 Strahan, S., Wang, Y., Froidevaux, L. and Degenstein, D.: Validation of SAGE III/ISS Solar
1179 Occultation Ozone Products With Correlative Satellite and Ground-Based Measurements. Journal
1180 of Geophysical Research: Atmospheres, 125(11), p.e2020JD032430, 2020.

1181

1182 Wang, W., Cheng, T., van der A, R.J., de Laat, J. and Williams, J.E.: Verification of the
1183 Atmospheric Infrared Sounder (AIRS) and the Microwave Limb Sounder (MLS) ozone algorithms
1184 based on retrieved daytime and night-time ozone, Atmos. Meas. Tech., 14(2), pp.1673-1687, 2021.

1185

1186 Zhang, L., Jacob, D.J., Liu, X., Logan, J.A., Chance, K., Eldering, A. and Bojkov, B.R.:
1187 Intercomparison methods for satellite measurements of atmospheric composition: application to
1188 tropospheric ozone from TES and OMI. Atmospheric Chemistry and Physics, 10(10), pp.4725-
1189 4739, 2010.

1190

1191 Zhu, T., W. Lin, Y. Song, X. Cai, H. Zou, L. Kang, L. Zhou, and H. Akimoto: Downward transport
1192 of ozone-rich air near Mt. Everest, Geophys. Res. Lett., 33, L23809, doi:10.1029/2006GL027726,
1193 2006.

1194

1195 Ziemke, J.R., Chandra, S. and Bhartia, P. K.: Two new methods for deriving tropospheric column
1196 ozone from TOMS measurements: Assimilated UARS MLS/HALOE and convective-cloud
1197 differential techniques, J. Geophys. Res. Atmos., 103(D17), pp.22115-22127, 1998.

1198

1199 Ziemke, J.R., Chandra, S., Duncan, B.N., Froidevaux, L., Bhartia, P.K., Levelt, P.F. and Waters,
 1200 J.W.: Tropospheric ozone determined from Aura OMI and MLS: Evaluation of measurements and
 1201 comparison with the Global Modeling Initiative's Chemical Transport Model, J. Geophys. Res.
 1202 Atmos., 111(D19), 2006.

1203

1204 ~~Zhang, R., Wang, H., Qian, Y., Rasch, P.J., Easter, R.C., Ma, P.L., Singh, B., Huang, J. and Fu,~~
 1205 ~~Q.: Quantifying sources, transport, deposition, and radiative forcing of black carbon over the~~
 1206 ~~Himalayas and Tibetan Plateau. Atmospheric Chemistry and Physics, 15(11), pp.6205–6223, 2015.~~

1207

1208

1209

1210

1211

1212

1213

1214

1215 **Table 1.** The mean values and corresponding standard errors of ozone mixing ratio (ppbv) from
 1216 ozonesonde, ozonesonde (AK) and AIRS over Nainital at six pressure levels and during winter,
 1217 spring, summer-monsoon, autumn are given. The number of ozonesonde flights during four
 1218 seasons are mentioned in the bracket.

Pressure levels	706 (hPa)	496 (hPa)	300 (hPa)	103 (hPa)	29 (hPa)	14.4 (hPa)
ozonesonde	55.1±0.9	54.4±0.7	69.5±2.8	238.8±15.0	4569.3±67.8	7620.6±140.1

Winter (61)	ozonesonde (AK)	48.6±0.4	55.9±0.6	70.4±1.8	187.3±3.6	5249.1±78.8	8214.9±105.7
	AIRS	46.5±0.3	52.2±0.6	68.7±1.2	354.4±8.4	4428.2±55.8	6616.4±56.0
Spring (72)	ozonesonde	71.6±1.8	70.2±1.5	81.5±2.8	223.9±12.7	4747.0±42.6	8242.3±101.6
	ozonesonde (AK)	58.7±0.7	69.1±1.1	80.3±1.4	221.8±3.6	5137.8±63.4	8784.4±96.6
	AIRS	55.3±0.4	60.7±0.7	78.6±1.0	389.2±6.0	4687.4±38.2	7852.4±97.0
Summer- monsoon (55)	ozonesonde	53.0±2.7	65.1±2.7	82.1±2.5	138.6±3.4	4642.9±26.4	8493.6±91.1
	ozonesonde (AK)	44.1±1.2	62.3±1.7	68.7±1.7	224.3±3.4	5271.3±44.6	9233.8±72.4
	AIRS	48.8±0.5	57.5±0.5	63.6±0.6	267.4±5.5	4710.0±48.2	8333.1±82.5
Autumn (54)	ozonesonde	53.0±1.1	63.8±1.6	72.7±1.6	144.6±6.2	4439.3±28.2	8613.7±77.5
	ozonesonde (AK)	50.4±0.5	61.0±0.8	64.1±0.9	169.0±2.0	5086.3±38.7	9035.8±80.7
	AIRS	46.0±0.3	51.3±0.4	56.9±30.5	241.8±3.6	4635.4±43.9	7984.9±97.6

1219 **Table 2.** Coefficient of determination (r^2) of three IR satellite sensors (AIRS, IASI and CrIS) ozone
1220 retrieval in five broad layers with respect to ozonesonde observations.

	Coefficient of determination (r^2)		
	AIRS	IASI	CrIS
600 - 800 hPa	0.52	0.34	0.09

300 - 600 hPa	0.44	0.31	0.22
100 - 300 hPa	0.45	0.44	0.45
50-100 hPa	0.87	0.76	0.82
10 - 50 hPa	0.94	0.80	0.94

1221

1222

1223 **Table 3.** Total column ozone (TCO) differences in DU between AIRS, OMI and ozonesonde,
 1224 during twelve months.

TCO Diff. (DU)	Jan	Feb	Mar	Apr	May	Jun	Jul	Aug	Sep	Oct	Nov	Dec
AIRS-OMI	-3.9	2.2	-1.8	13.2	16.7	18	-2.2	17.2	22.1	13.2	0.0	-2.7
AIRS- ozonesonde	-2.1	3.5	6.0	8.1	19.4	11.8	-2.3	22.3	21.6	15.0	5.6	5.2

1225

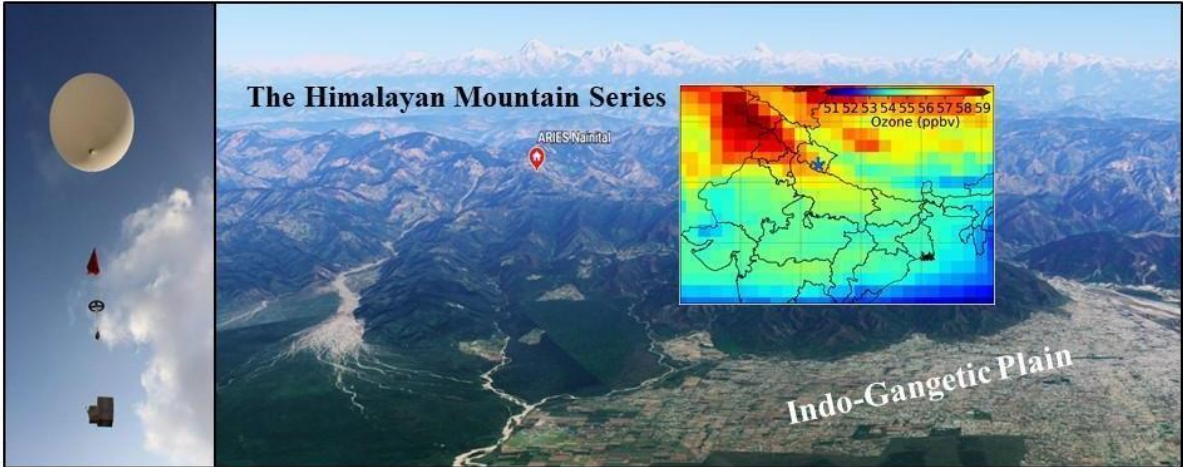
1226

1227

1228

1229

1230



1231

1232 **Figure 1.** Location (red color circle) of the balloon launching site (© Google Earth, 2021) situated
 1233 in the Aryabhata Research Institute of Observational Sciences (ARIES) (29.4° N, 79.5° E, and
 1234 1793 m elevation), Nainital in the central Himalaya. The spatial distribution of ozone (AIRS) at
 1235 500 hPa is also shown over northern India and the location of the site is marked with a blue star.
 1236 A photo of balloon, together with parachute, unwinder, ozonesonde along with GPS-radiosonde
 1237 above the observation site is also shown at the left.

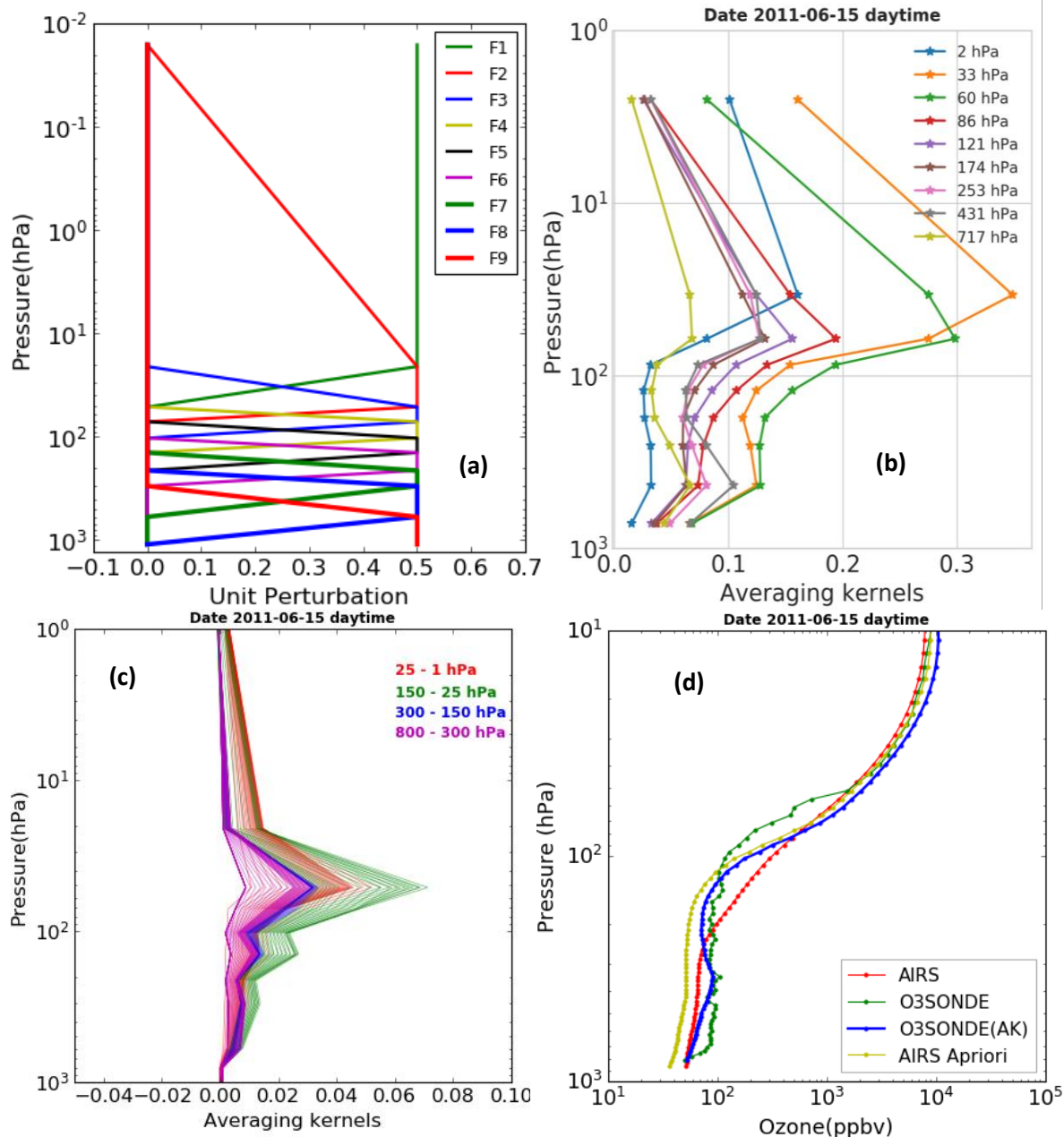
1238

1239

1240

1241

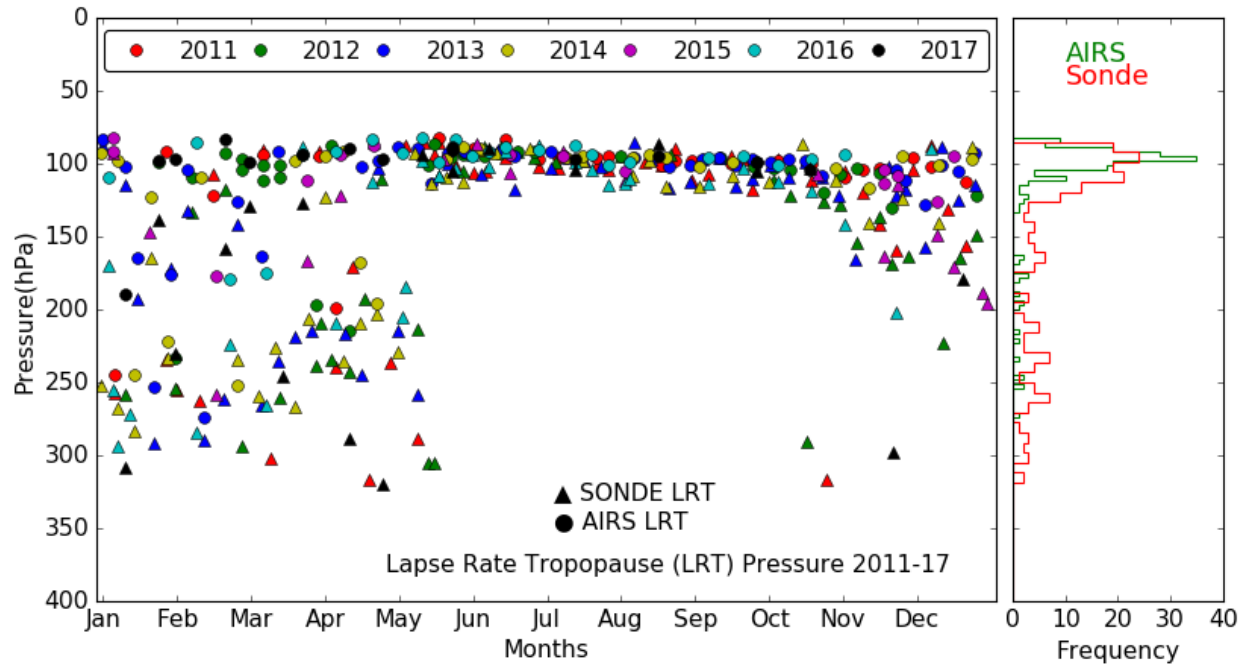
1242



1243

1244
1245

1246 **Figure 2.** (a) Nine trapezoid functions used for ozone retrieval in AIRS-V6. (b) AIRS ozone
1247 averaging kernel matrix over Nainital at 9 levels vertical grid. (c) Calculated AIRS averaging
1248 kernel matrices at 100 RTA grids after applying the trapezoid function. (d) An example of ozone
1249 profiles using different data sets for 15 June, 2011 over the observation site.



1250

1251 **Figure 3.** Lapse rate tropopause pressure monthly variation from balloon-borne and AIRS
 1252 observations and respective frequency distributions during 2011 - 2017.

1253

1254

1255

1256

1257

1258

1259

1260

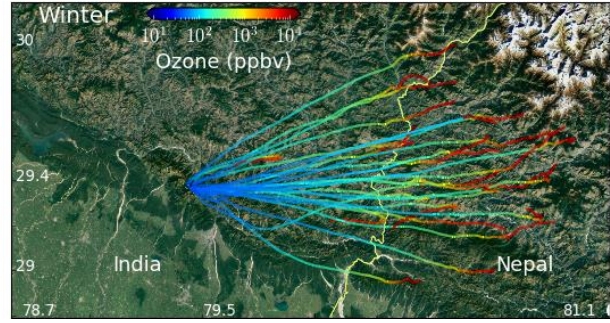
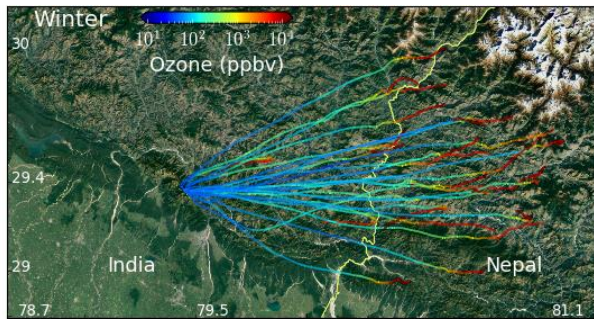
1261

1262

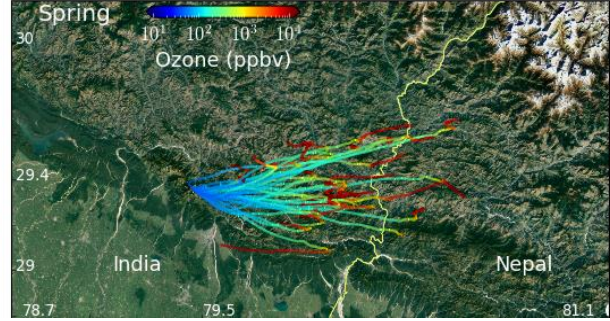
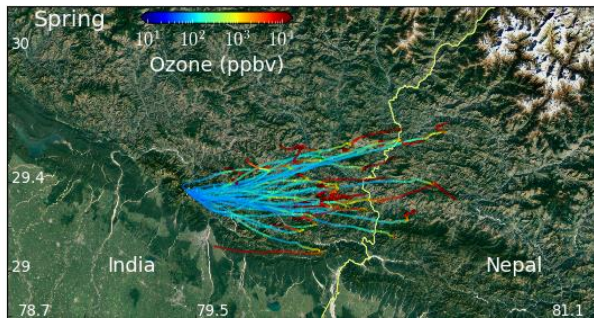
1263

Ozonesonde

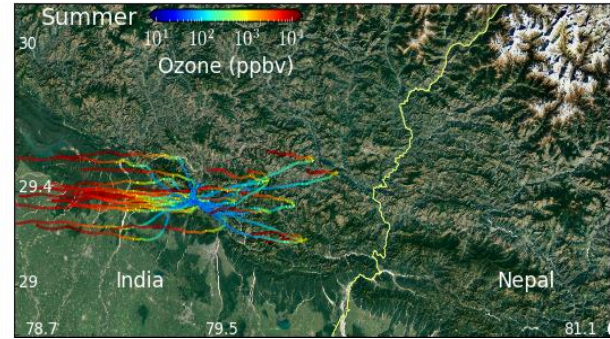
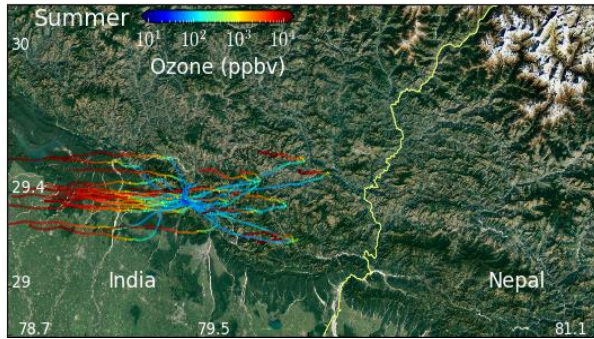
AIRS



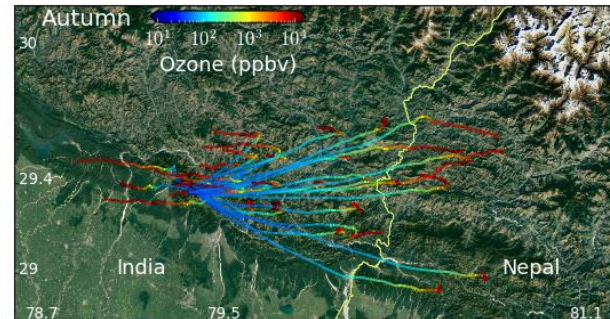
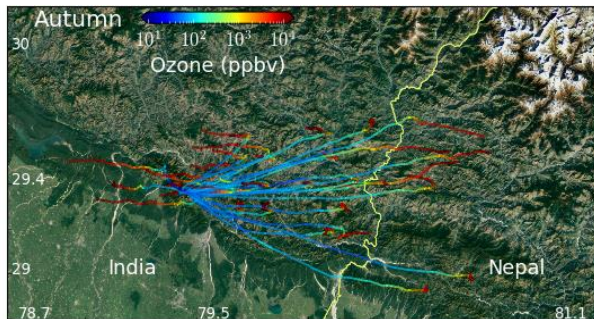
1264



1265



1266



1267

1268

1269

1270

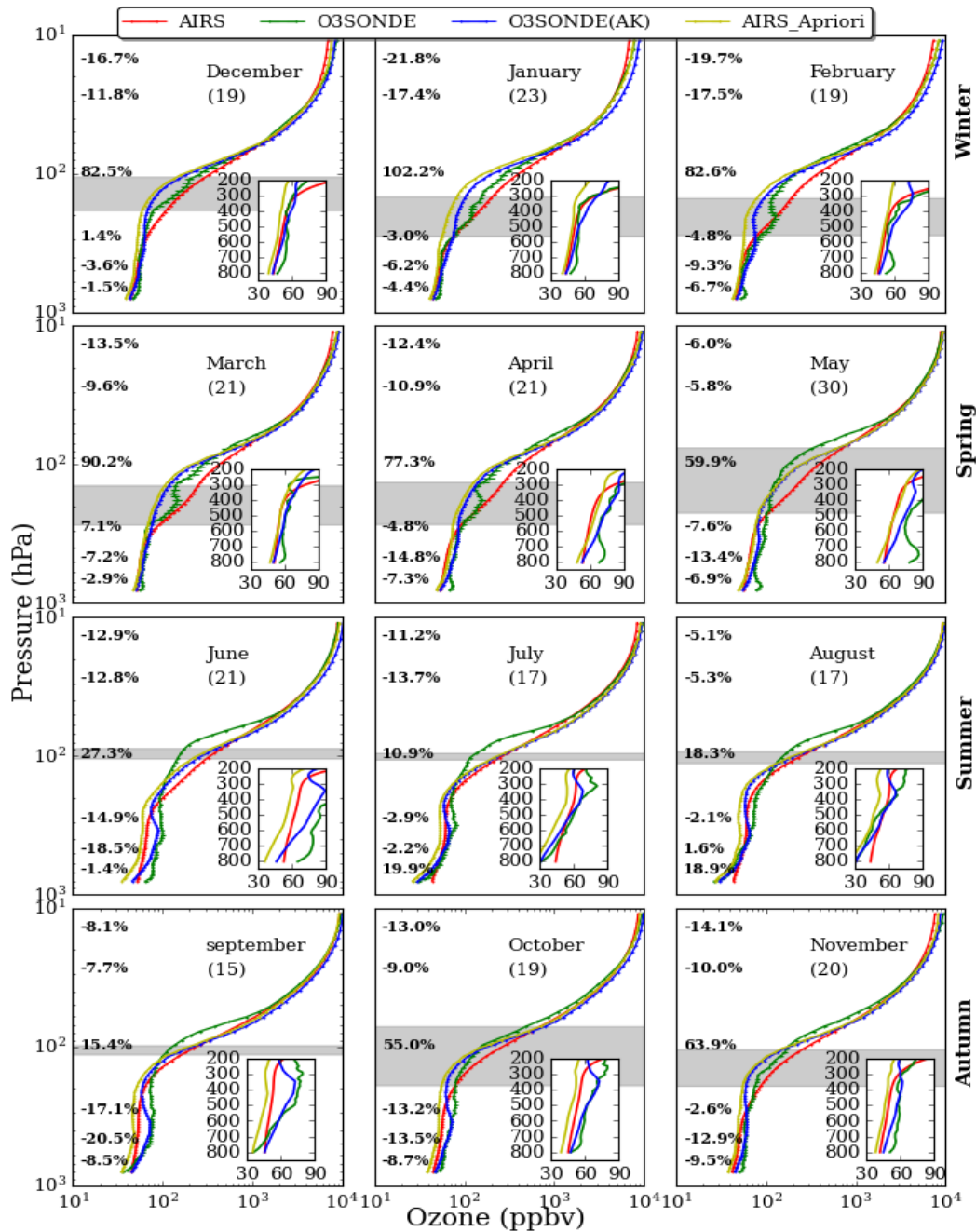
1271

1272

1273

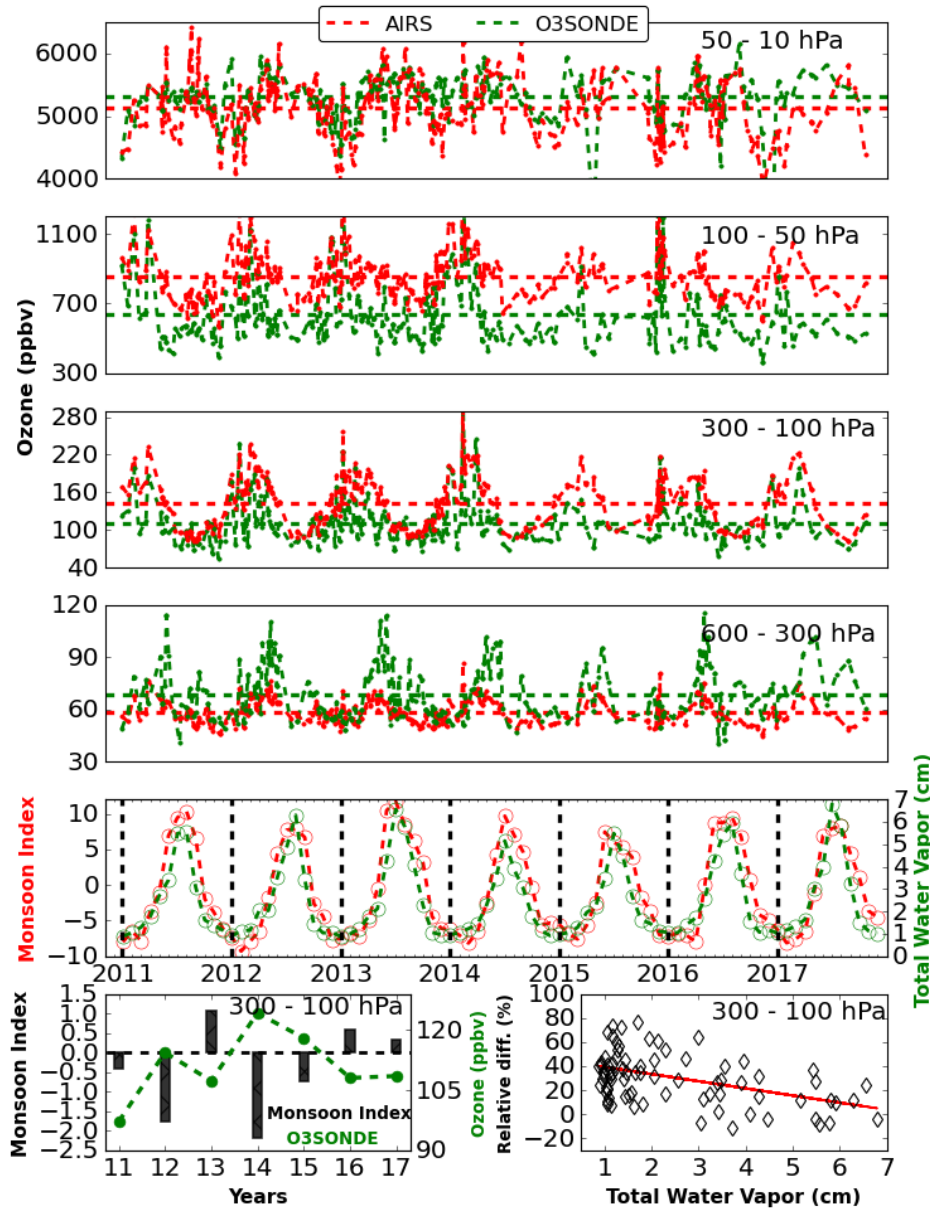
1274

Figure 4. Spatial distribution of ozone using all ozone soundings (left) launched from ARIES, Nainital, India (© Google Earth, 2021) along with the balloon trajectories. Ozone spatial distribution from AIRS (right), following the balloon tracks, is also shown. It could be seen that the balloon reaches Nepal many times in the autumn and winter seasons.



1275

1276 **Figure 5.** Monthly averaged (2011-2017) ozone profiles of ozonesonde, AIRS, ozonesonde (AK)
 1277 and AIRS a-priori over Nainital in the central Himalaya. The percentage difference $[(\text{AIRS} -$
 1278 $\text{ozonesonde (AK)})/\text{ozonesonde (AK)}] \times 100$ at 706, 496, 300, 103, 29, and 14.4 hPa are also written
 1279 at respective altitudes. The standard error corresponding to each profile is also shown with error
 1280 bars. The number of ozonesonde for different months is written in the bracket and grey shaded
 1281 area shows the tropopause (mean \pm sigma) from balloon-borne observations.

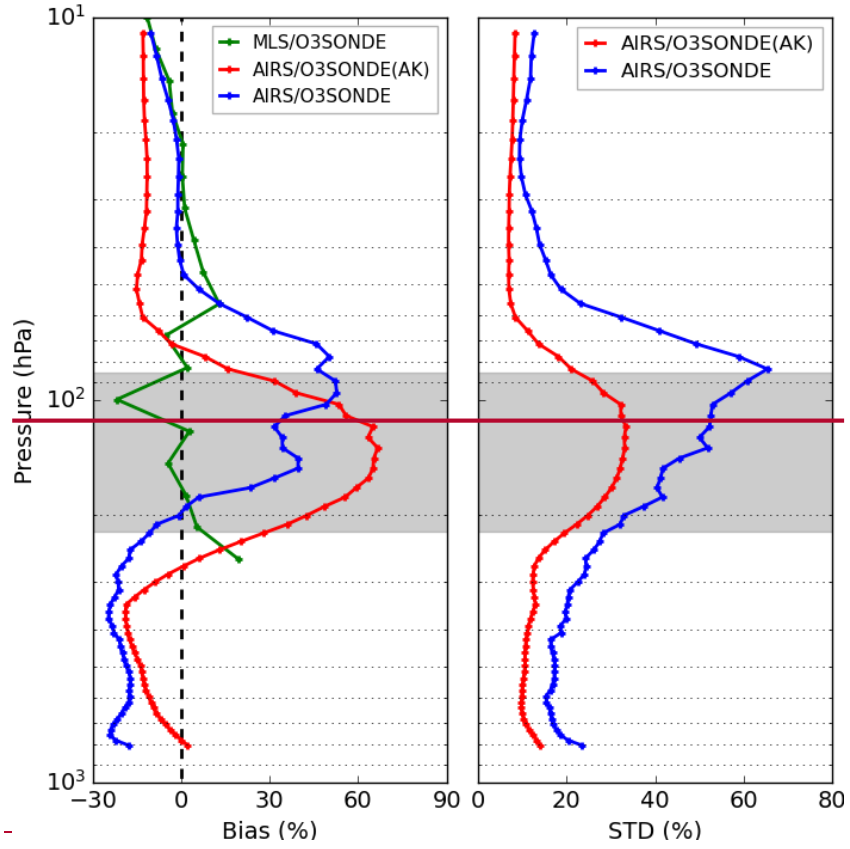


1282

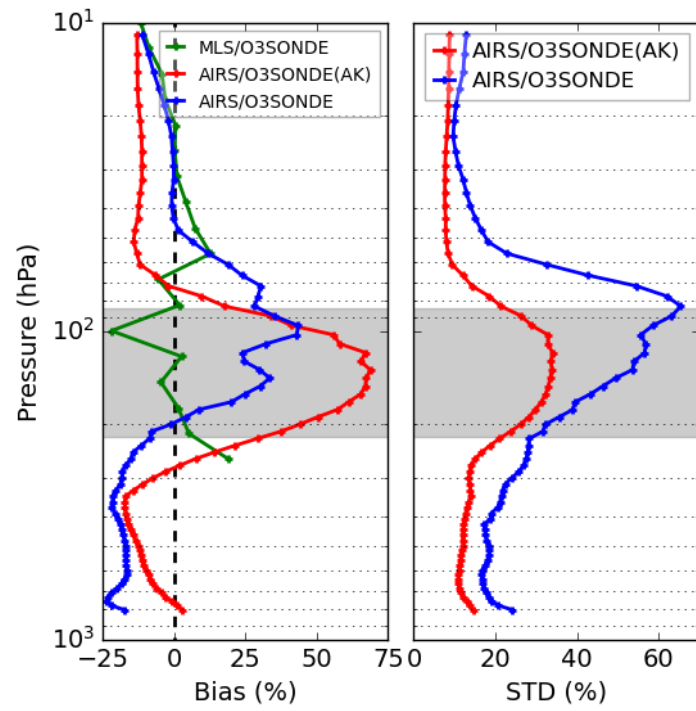
1283 **Figure 6.** Average variations in ozone mixing ratios at four defined layers, characterizing the
 1284 middle stratosphere (50 - 10 hPa), the lower stratosphere (100 - 50 hPa), the upper troposphere
 1285 (300 - 100 hPa), and the middle troposphere (600 - 300 hPa), respectively. The red and green dash
 1286 horizontal lines show the average ozone mixing ratios in the defined layers from AIRS and
 1287 ozonesonde, respectively, from 2011 to 2017. The monthly variation of the total column water
 1288 vapor (cm) along with the monsoon index is also shown. The yearly average ozone from
 1289 ozonesonde and monsoon index (bar plot) for different years (left lower most) and scattered plot
 1290 of ozone relative difference (%) $[(AIRS-O3SONDE)/O3SONDE]*100$, with total water vapor
 1291 (right lower most) in the upper troposphere (300 - 100 hPa) are also shown.

1292

1293

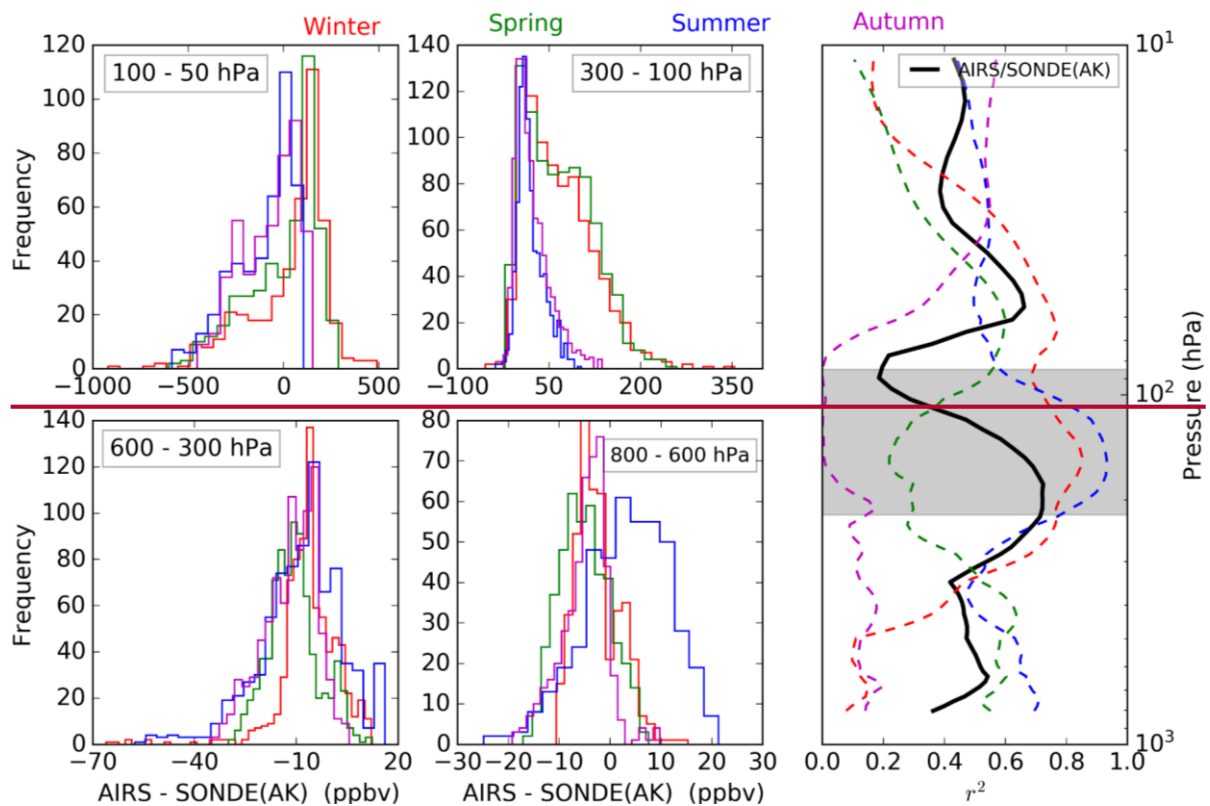


1294



1295 **Figure 7.** Statistical error analysis (Bias and standard deviation) of AIRS retrieved ozone with
 1296 ozonesonde and ozonesonde (AK) for collocated data of seven years (2011 - 2017). The Bias
 1297 between collocated data of MLS (261 hPa - 10 hPa) and ozonesonde over Nainital during 2011 -
 1298 2017 is also shown with the green profile. The grey shaded area shows the tropopause region from
 1299 balloon-borne radiosondes observations.

1300



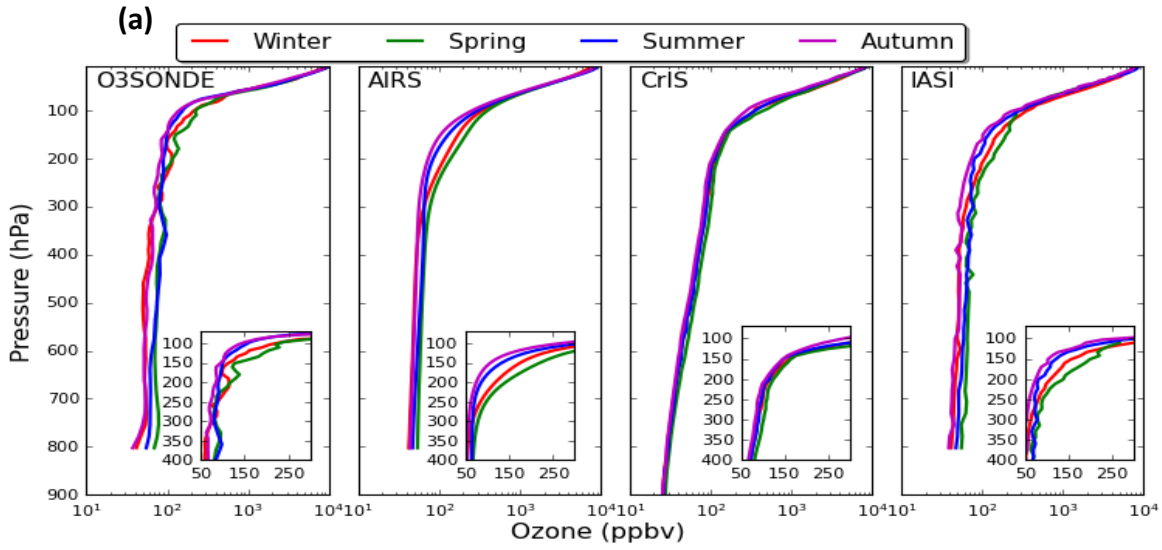
1301

1302 **Figure 8.** Histogram difference between AIRS ozone and ozonesonde (AK) in the four defined
 1303 layers. The average correlation profiles between AIRS ozone and ozonesonde (AK) are shown on
 1304 the right during winter (red), spring (green), summer monsoon (blue), and autumn (magenta). The
 1305 black line is for the entire data set. The grey shaded area shows the tropopause region from balloon-
 1306 borne radiosondes observations.

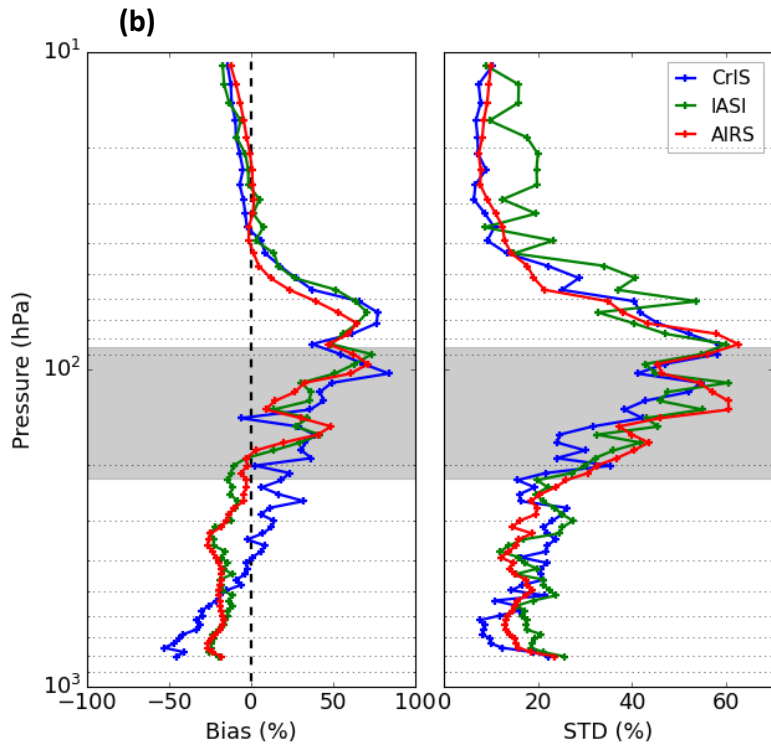
1307

1308

1309



1310
1311



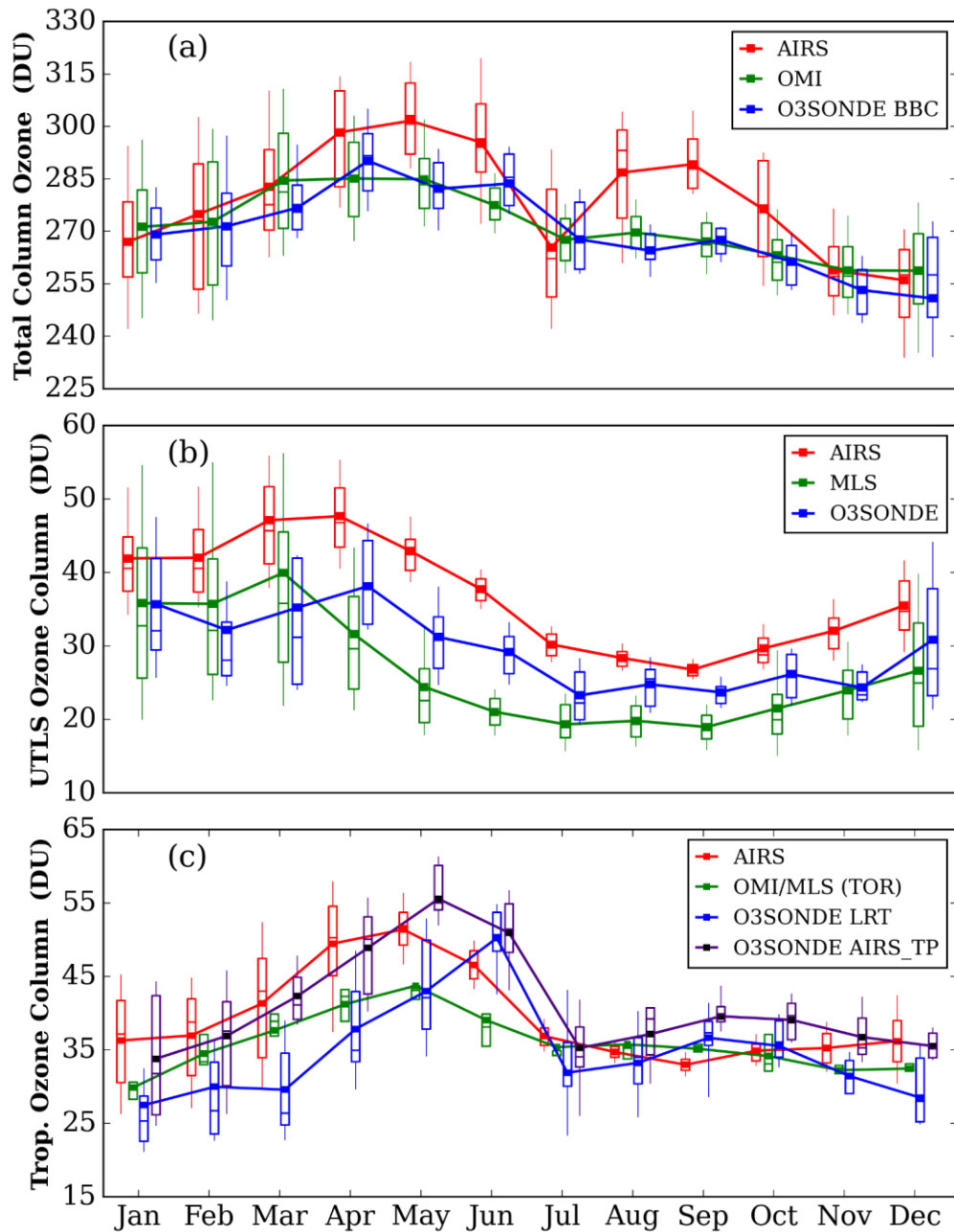
1312

1313

1314

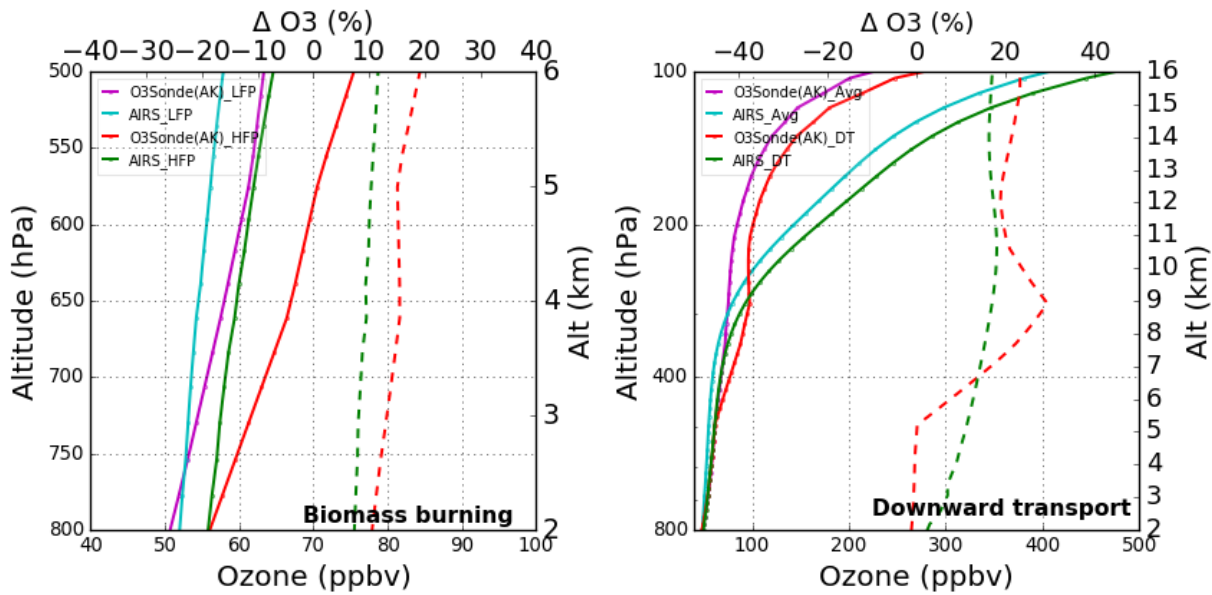
Figure 98. (a) Seasonal ozone profiles of three IR satellites (IASI, AIRS, and CrIS) for a smaller sample size (April 2014 to April 2015). The IASI and CrIS products are generated using the AIRS

1315 heritage algorithm (NOAA) and only zero quality flags (QC=0) of retrieval are used. (b) Statistical
 1316 error analysis for the three IR satellites retrieved ozone without applying the averaging kernel
 1317 information. The grey shaded area shows the tropopause region from balloon-borne observations.



1318
 1319 **Figure 109.** (a) Monthly average variations of total column ozone (TCO) for AIRS, OMI, and
 1320 ozonesonde (Balloon Burst Climatology) over the central Himalaya for the 2011-2017 period. (b)
 1321 Monthly average variation of UTLS ozone column for AIRS, MLS, and ozonesonde, over the

1322 central Himalayas for the 2011-2017 period. (c) Monthly average variations of tropospheric ozone
 1323 column of AIRS, OMI/MLS (Tropospheric Ozone Residual), and ozonesonde (LRT - sonde lapse
 1324 rate) over the central Himalayas for the 2011-2017 period. The ozonesonde tropospheric ozone
 1325 column is also shown using AIRS tropopause (AIRS_TP). In the box plot, the lower and upper
 1326 edges of the boxes represent the 25th and 75th percentiles. The whiskers below and above are 10th
 1327 and 90th percentiles.
 1328



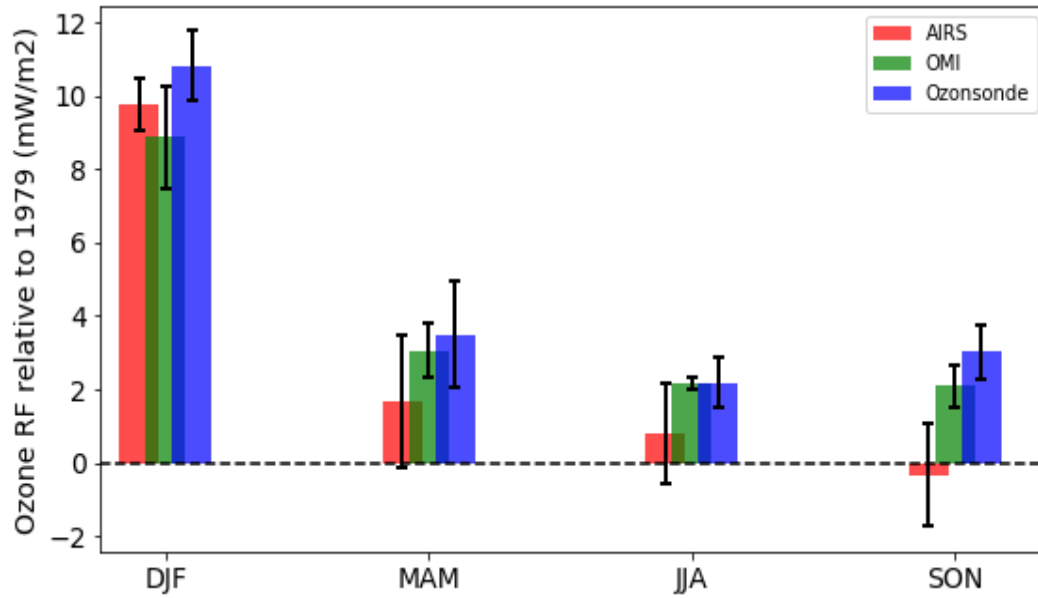
1329
 1330 **Figure 11.** (a) Vertical ozone profiles of AIRS ozone and ozonesonde (AK) during low fire
 1331 period (LFP) and high fire period (HEP). The solid lines correspond to ozone profiles while the
 1332 dotted lines show a percentage increase in ozonesonde (red) and AIRS (green) profiles during
 1333 biomass burning events. (b) Vertical ozone profiles of AIRS ozone and ozonesonde (AK) during
 1334 events of downward transport. The dotted line shows ozone enhancement during downward
 1335 transport events.

1336

1337

1338

1339



1340

1341 **Figure 1211.** Seasonal average ozone UV radiative forcing (RF) relative to 1979 as calculated
 1342 from ozonesonde, OMI, and AIRS total ozone data for the 2011 - 2017 period. Spreads correspond
 1343 to one standard deviation.

1344